

ULSR-GS: Urban Large-scale Surface Reconstruction Gaussian Splatting with Multi-View Geometric Consistency

Zhuoxiao Li ^{†a,c}, Shanliang Yao^{†a,e}, Yong Yue^a, Wufan Zhao^b, Rongjun Qin^d, Ángel F. García-Fernández^{f,c}, Andrew Levers^{c,g} and Xiaohui Zhu ^a

^aSchool of Advanced Technology, Xi'an Jiaotong-Liverpool University, Suzhou, 215123, China

^bUrban Governance and Design Thrust, The Hong Kong University of Science and Technology (Guangzhou), Guangzhou, 511453, China

^cDepartment of Electrical Engineering and Electronics, University of Liverpool, Liverpool, L69 3GJ, UK

^dDepartment of Civil, Environmental and Geodetic Engineering, The Ohio State University, Columbus, OH 43210, USA

^eSchool of Information Engineering, Yancheng Institute of Technology, Yancheng, 224051, China

^fIPTC, ETSI de Telecomunicación, Universidad Politécnica de Madrid, Madrid, 28040, Spain

^gInstitute for Digital Engineering and Autonomous Systems, University of Liverpool, Liverpool, L69 3GJ, UK

ARTICLE INFO

Keywords:

Surface Reconstruction
Gaussian Splatting
Large-Scale Scenes
Aerial Photogrammetry
Urban Scene Reconstruction

ABSTRACT

Recent advances in 2D Gaussian Splatting (2DGS) have demonstrated compelling rendering efficiency and mesh extraction capabilities. However, its application to large-scale aerial photogrammetry, especially using oblique UAV imagery, remains limited due to three primary challenges: (1) suboptimal image selection in scene partitioning strategies failing to scale effectively; (2) densification pipelines that rely primarily on single-view constraints resulting in over-smoothed reconstructions and loss of fine geometric detail; and (3) the absence of multi-view geometric consistency constraints leading to surface artifacts and inconsistencies. To address these limitations, we propose ULSR-GS, a novel method tailored for high-resolution surface reconstruction in urban-scale environments. Firstly, we propose a point-to-photo partitioning strategy that segments the scene based on the sparse SfM point cloud and assigns only the most relevant images to each sub-region, which resolves key scalability bottlenecks. Secondly, we propose a multi-view guided densification strategy that enforces adaptive geometric consistency across views, overcoming the limitations of single-view-based densifications. Lastly, we introduce consistency-aware loss functions that explicitly regulate depth and normal alignment across views, significantly enhancing surface fidelity. Extensive experiments on large-scale aerial benchmark datasets demonstrate that ULSR-GS consistently outperforms existing single- and multi-GPU Gaussian Splatting methods. Furthermore, compared to MVS pipelines, our approach achieves comparable or superior geometric quality while being substantially more time-efficient, making it a practical solution for scalable 3D modeling in digital twin and urban mapping applications. Project page: <https://ulsr.gs.github.io>.

1. Introduction

High-fidelity 3D surface reconstruction at urban scale remains a longstanding challenge in photogrammetry and computer graphics, with critical applications in urban planning, simulation, and digital twins [51, 42, 12]. Traditionally, urban-scale surface reconstruction from aerial oblique imagery has relied heavily on Multi-View Stereo (MVS) techniques [44, 24, 56, 57, 3, 59, 71, 41, 32, 60, 14, 31, 70, 28], which reconstruct dense point clouds from image correspondences and subsequently extract meshes through surface reconstruction algorithms, such as Poisson Surface Reconstruction [17, 18] or Delaunay triangulation-based methods [23]. While effective, these traditional pipelines often encounter computational inefficiencies when scaling to urban-scale datasets comprising thousands of high-resolution images. Recent advancements in novel view synthesis (NVS) have led to from Neural Radiance Fields (NeRFs) [58, 69, 4, 1, 2] to the emergence of 3D Gaussian Splatting (3DGS) [19], a breakthrough approach enabling fast photorealistic rendering quality with unprecedented efficiency by directly

optimizing sparse 3D Gaussian primitives. In addition to achieving compelling visual realism, recent studies have demonstrated that 3DGS and its variants can serve as effective tools for extracting geometry-rich meshes [16, 5, 27].

Scaling Gaussian Splatting (GS) to city-scale surface reconstruction tasks is both an engineering and algorithmic challenge. Issue (1): The vanilla GS training pipeline [19, 16, 64, 66] does not inherently support multi-GPU parallel processing. For instance, even high-performance GPUs like the RTX 4090 (24GB VRAM) can manage only approximately 8 million primitives, limiting applications to relatively small datasets such as the Mip-NeRF 360 dataset [2]. Consequently, current large-scale GS approaches predominantly rely on a divide-and-conquer strategy by partitioning extensive scenes into smaller sub-scenes based on camera projections or clustering of camera poses obtained from Structure-from-Motion (SfM), subsequently distributing these partitions across multiple GPUs [29, 20, 9, 33, 34]. While effective for controlled, uniform camera distributions such as five-directional aerial surveys [35, 54], these image-based methods struggle with close-range oblique photogrammetry

*Corresponding author: Xiaohui.Zhu@xjtlu.edu.cn

**†Equal Contribution

ORCID(s):

scenarios, where irregular and complex camera trajectories result in uneven or inadequate training data distribution. Issue (2): Existing approaches necessitate merging sub-scenes before mesh extraction, a process requiring substantial computational resources. For example, methods employing TSDF fusion with a 0.2-meter voxel size consume over 300GB RAM for reconstructing merely 1,000 images, making scalability to city-scale scenes with tens of thousands of images impractical. Additionally, extracting meshes separately introduces further complications, such as determining optimal sub-scene boundaries, often leading to unnecessary computational overhead and fragmented meshes. Issue (3): Another significant challenge in GS-based large-scale reconstruction is the densification problem. GS explicitly represents scenes using discrete Gaussian primitives, meaning the richer and denser the primitives, the more accurately high-frequency geometric details can be captured [64, 10, 27, 13]. However, GS often struggles with accurately reconstructing low-frequency or textureless regions, resulting in incomplete or overly smooth surfaces [16, 13, 5]. Issue (4): Existing GS-based methods predominantly utilize single-view geometric consistency constraints during training [64, 10, 27, 13], which fail to leverage comprehensive multi-view information. This single-view approach can cause inconsistencies and inaccuracies, such as floaters or misaligned primitives, particularly in complex urban scenarios.

To address these critical issues, we propose ULSR-GS. Our key insight is combining detail-preserving optimization within each divided sub-region and enforcing multi-view consistency during training, which makes it possible for 2DGS to independently reconstruct each tile with high geometric fidelity. These sub-regions can then be seamlessly integrated into a globally consistent urban-scale surface without additional fusion or post-processing steps. Unlike other methods that partition scenes solely by camera positions [33, 67, 29, 34], we propose a point-to-photo partitioning strategy driven by the spatial distribution of sparse SfM points and their associated views. For each candidate sub-region, we meticulously select an optimal subset of images for each SfM point, ensuring comprehensive and relevant coverage. We then introduce a multi-view constrained densification approach within the optimization process for each partitioned sub-region. This strategy explicitly enforces geometric consistency across multiple views by penalizing discrepancies in depth and normal orientations of corresponding points across different images. Consequently, our multi-view densification preserves essential fine details, which are preserved when sub-regions are optimized independently. Collectively, the innovative integration of our point-to-photo partitioning and multi-view densification strategies positions ULSR-GS as a highly effective and scalable solution for accurate and detailed large-scale urban surface reconstructions.

Our contributions are summarized as follows:

- We present ULSR-GS, a novel method specifically designed to overcome the limitations of existing GS-based works in large-scale surface reconstruction tasks.

- A partitioning strategy that supports extracting the geometry of each trained GS sub-region separately, without the need for merging and then extracting.
- An densification method based on multi-view depth aggregation, which can improve rendering and geometry reconstruction quality.
- Two efficient multi-view consistency constraints for generating detailed and accurate reconstructions in large-scale urban environments.

2. Related work

2.1. Large-Scale Novel View Synthesis

Recent developments in novel view synthesis [1, 7, 69, 39] include several innovative approaches tailored for large-scale environments [53, 46, 38, 47]. BungeeNeRF first addresses the challenge of rendering city-scale scenes with drastic scale variations by introducing a progressive neural radiance field that adapts to different levels of detail [53]. BlockNeRF segments a city into distinct blocks and strategically allocates training views based on their spatial locations [46]. Mega-NeRF takes a grid-based approach, assigning each pixel in an image to various grids corresponding to the rays it traverses [47]. In contrast to these partitioning methods, Switch-NeRF employs a mixture-of-experts framework that facilitates scene decomposition, allowing for more nuanced representation [38]. Grid-NeRF, while not focusing on scene decomposition, combines NeRF-based techniques with grid-based methodologies to enhance rendering efficiency [55].

Moreover, the adoption of 3D Gaussian Splatting [19] has emerged as a promising approach, improving both reconstruction accuracy and rendering speed [64, 37, 11]. GS-based large-scale rendering methods primarily handle large-scale scene rendering through camera-position-based partitioning, followed by point cloud selection or segmentation [29, 67, 33, 20, 6]. This strategy ensures that training images for each region remain as similar as possible, enabling efficient techniques like Level of Detail (LOD) to accelerate rendering [33, 20, 6]. This partitioning approach is particularly effective for terrestrial sequences [20] and aerial five-directional oblique photography [29, 67, 6]. However, when dealing with scenarios involving specific path planning algorithms, these partitioning methods may struggle to adapt efficiently, leading to suboptimal training data distribution and reduced reconstruction quality for dynamically changing viewpoints.

2.2. 3D Surface Reconstruction

3D reconstruction has evolved from traditional Multi-View Stereo (MVS) [44, 24, 56, 57, 3, 59, 71, 41, 32, 60, 14, 31, 70, 28] to advanced neural methods [49, 40, 63], and mesh extraction methods transform implicit representations into explicit 3D models. Poisson Surface-based methods extract surfaces from point clouds but often produce overly smooth results, lacking fine details [15]. Marching Cubes

converts volumetric data into polygonal meshes, but its grid-based nature can lead to artifacts and increased memory usage [36, 27]. Neural implicit representations encode 3D geometry continuously, enabling smooth modeling and handling complex topologies [49, 63, 62]. However, these methods require significant computational resources and often struggle with fine geometric details. Mesh extraction from these representations also suffers from discretization artifacts. Neural Radiance Fields (NeRF) use volumetric rendering to achieve high-quality view synthesis [39]. Despite their impressive results, NeRF-based methods are computationally intensive, making them less practical for real-time applications [1, 47]. Recent works extract explicit geometry from NeRF, but converting density fields to surfaces in large-scale scenes remains challenging and may produce noisy results [26].

Some research has begun to explore mesh extraction using 3DGS [19]. Early work combined 3DGS with Poisson Surface Reconstruction to achieve reconstruction [15]. Subsequently, studies used rendered depth maps with Truncated Signed Distance Function (TSDF) fusion to reconstruct surfaces [50], [48], improving accuracy by modifying the depth calculation method [16, 68, 5, 27], and optimizing the densification process during training [13, 27]. Additionally, a study utilized Gaussian opacity fields combined with a marching tetrahedra approach to achieve high-quality reconstruction results [66]. Existing GS-based methods perform inadequately in large-scale scenes, struggling to accurately reconstruct intricate geometric details and prone to generating significant artifacts. Using the partition rendering methods [29, 33, 25] to split the scene into different sub-regions can solve this problem well, and each sub-region can obtain sufficient densification. However, the current partitioning methods lack optimization of the mesh extraction task and usually require mesh extraction after merging the entire scene.

3. Preliminaries

3.1. Multi-View Pair Selection

The *multi-view pair selection* utilizes a reference image along with three source images ($N = 3$) [52, 61, 65, 45, 8]. For each image pair, they calculate a score $s(i, j)$ based on sparse points. The score is defined as:

$$s(i, j) = \sum_p G(\theta_{ij}(p)) \quad (1)$$

where p represents a common track point in both views i and j , and $\theta_{ij}(p)$ is the baseline angle between the views.

The function G is a piecewise Gaussian function that favors a certain baseline angle θ_0 :

$$G(\theta) = \begin{cases} \exp\left(-\frac{(\theta-\theta_0)^2}{2\sigma_1^2}\right), & \theta \leq \theta_0 \\ \exp\left(-\frac{(\theta-\theta_0)^2}{2\sigma_2^2}\right), & \theta > \theta_0 \end{cases} \quad (2)$$

3.2. Depth Calculation in 2D Gaussian Splatting

In 2DGS [16], two methodologies are employed for aggregating depth information.

Weighted aggregation. For each Gaussian G_i intersecting along a viewing ray, the depth D_{mean} is computed as a weighted sum:

$$D_{mean} = \sum_i \omega_i D_i / (\sum_i \omega_i + \epsilon) \quad (3)$$

where ω_i represents the weight contribution of the i -th Gaussian. The result is normalized by the cumulative alpha values to obtain the expected depth.

Maximum visibility. This method focuses on selecting the depth of the most "visible" Gaussian along the viewing ray. The depth D_{median} is determined by the first Gaussian that contributes significantly to the cumulative alpha:

$$D_{median} = \max \{z_i | T_i > 0.5\} \quad (4)$$

where T_i quantifies the visibility based on the i -th Gaussian's alpha value.

D_{mean} facilitates smoother depth calculations, whereas D_{median} more effectively captures rich geometric detail. However, it is highly susceptible to floating-point errors that can impact depth computation. In this paper, we adopt D_{mean} as the depth representation for subsequent analyses.

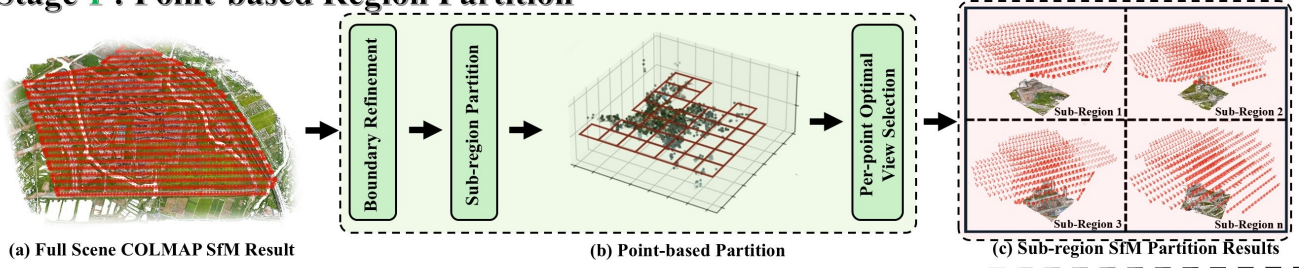
4. Method

Figure 1 illustrates the overall pipeline of our proposed ULSR-GS, which consists of three stages: **Stage 1: Multi-View Optimized Point Partitioning (Sec. 4.1)**. Starting from a full-scene COLMAP SfM result, we apply density-aware boundary refinement (Sec. 4.1.1) followed by spatial subdivision of the sparse point cloud into multiple rectangular sub-regions (Sec. 4.1.2). Each point is then assigned to its most informative image group via our proposed per-point optimal view selection, resulting in a well-structured sub-region configuration suitable for parallel processing (Sec. 4.1.4). **Stage 2: Sub-region Training.** Each sub-region is independently trained using 2DGS rasterization. Our training module includes an adaptive multi-view guided densification mechanism (Sec. 4.2), where source view depths are aggregated (Sec. 4.2.1) and reprojected to the reference view through an adapted window mask (Sec. 4.2.2). To enforce geometric consistency across depth and normal maps, we further introduce two multi-view regulations (Sec. 4.3). This enables accurate local optimization with fine-grained geometry reconstruction. **Stage 3: Sub-region Geometry Extraction.** After training, surface meshes for each sub-region are extracted using TSDF fusion followed by a cropping step. These independently reconstructed regions are then seamlessly assembled into a complete large-scale urban mesh without requiring additional global fusion.

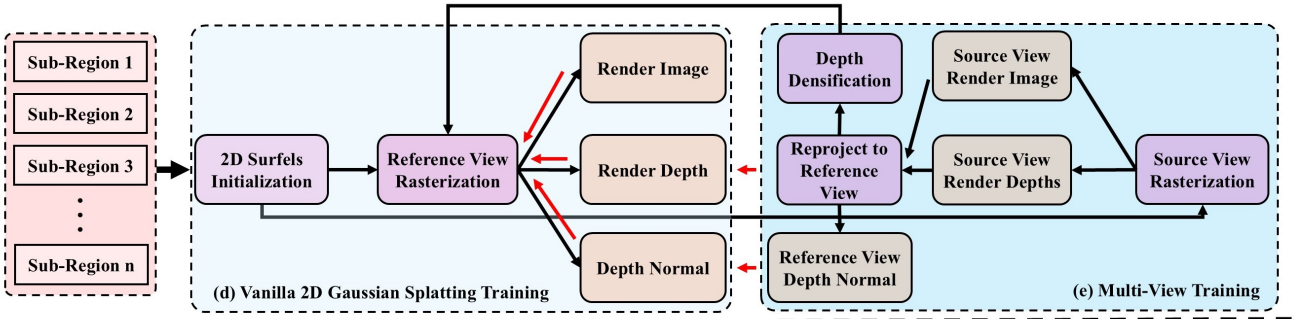
4.1. Multi-View Optimized Point Partitioning

In this section, we will detail the point-based scene partitioning method in Figure 1 **Stage 1** and the method to

Stage 1 : Point-based Region Partition



Stage 2: Sub-region Training



Stage 3: Sub-region Geometry Extraction

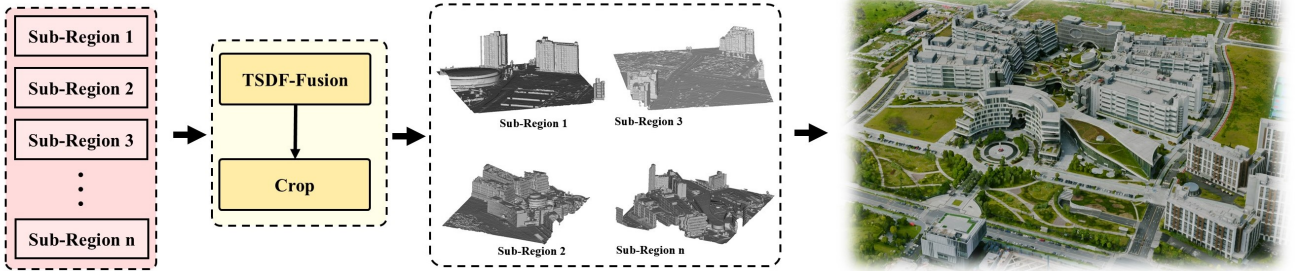


Figure 1: ULSR-GS training pipeline. Stage 1: Scene partitioning based on point cloud. Stage 2: Training strategy based on multi-view geometric consistency. Stage 3: Extract the geometry of sub-regions separately and seamlessly merge.

select views for the partitioned sub-regions. Different from previous studies that use drone photo locations for region partitioning [29, 67, 33], our scene partitioning method is based on the initial point cloud of the scene and selects the best training images for the point cloud in each sub-region. The advantage of this method is that we can determine the boundaries of the mesh to be extracted for each sub-area at the early stage, without the need to merge the full scene. As illustrated in Figure 2, we optimize the partition process by focusing on the most relevant parts of the scene.

4.1.1. Density-controlled boundary refinement.

To effectively partition the initial points into $n \times n$ sub-regions, it is crucial to isolate the primary structural components of the scene and eliminate sparse and noisy SfM points that could distort the boundary definition.

We first remove all 3D points with a SfM reprojection error [44] greater than a threshold ϵ_{error} ($\epsilon_{error} > 1.5$ in our experiments). This step cleans up the point cloud by discarding unreliable points that could skew the partitioning. Then we partition the 3D space into a voxel grid v_i with size

($s = 2$), and each SfM point $p_i = (x_i, y_i, z_i)$ is assigned to a voxel based on its coordinates:

$$v_i = \left(\left\lfloor \frac{x_i}{s} \right\rfloor, \left\lfloor \frac{y_i}{s} \right\rfloor, \left\lfloor \frac{z_i}{s} \right\rfloor \right). \quad (5)$$

For each voxel v , we count the number of points N_v it contains:

$$N_v = \sum_{i=1}^N \delta(v_i, v), \quad (6)$$

where N is the total number of points and $\delta(v_i, v)$ is the Kronecker delta function [22]. Then we compute a density threshold N_τ ($\tau = 33.3\%$) of the maximum voxel occupancy to identify the densely populated voxels:

$$N_\tau = \max_{v \in V} N_v. \quad (7)$$

Voxels with occupancy $N_v > N_\tau$ are considered dense and are retained. Finally, we can get the precise boundary of the scene by computing the minimum and maximum coordinates of the points.

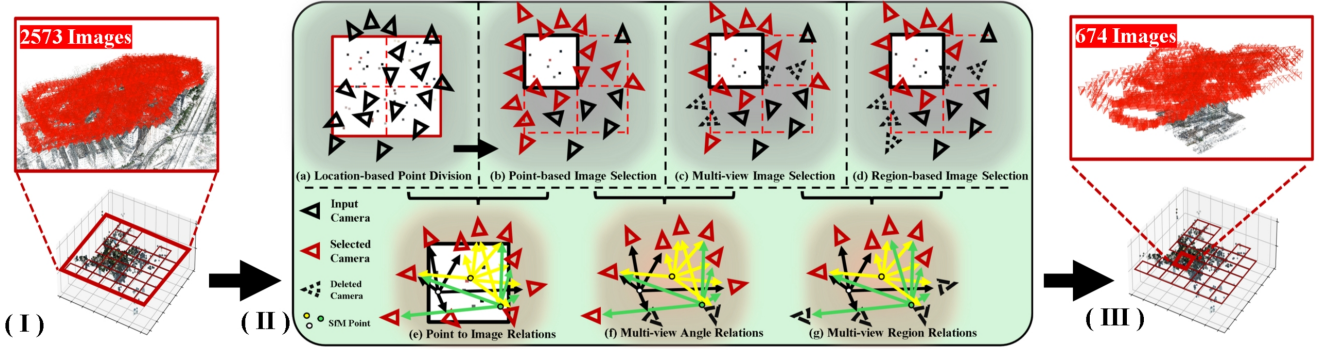


Figure 2: Point-based partition strategy of ULSR-GS. (I) We partition the training scene based on the positions of the point cloud projected onto the xz -plane. (II) For each sub-scene: (a) we first select all matching images within the region; (b) based on the camera relationships of the sub-scene, we select the corresponding images for each point; (c) following the principle of multi-view optimal matching [61], we filter out images with poor view angles; and finally, (d) considering the distance relationship, we further remove images that are too distant. (III) Examples of a sub-region significantly reduce the number of training images.

4.1.2. Initial view selection.

As shown in Figure 2 (I), the input COLMAP SfM [44] point cloud is divided into $n \times n$ grids after density filtering. Each point in the sub-region is the feature of the images in which it was detected and matched. We first select all matched images as a coarse view selection (see Figure 2 (e)).

4.1.3. Source view selection.

To further refine the view selection in Eq. (1), a region constraint is applied based on the camera pair distance d_{ij} . Only image pairs with a distance below a specified maximum threshold D_{\max} are considered for matching. The final matching score S_{ij} :

$$S_{ij} = \begin{cases} \sum_p G(\theta_{ij}(p)), & d_{ij} \leq D_{\max} \\ 0, & \text{otherwise} \end{cases} \quad (8)$$

Finally, for each reference image I_{ref_i} , the top 3 source images $I_{\text{src}_i^1}, I_{\text{src}_i^2}, I_{\text{src}_i^3}$ with the highest matching scores S_{ij} are selected to form the optimal set of views.

4.1.4. Per-point optimal view selection.

Our goal is to ensure that each SfM point within a sub-region is associated with its most informative and geometrically robust image pairs. For each point $P_k \in \mathcal{P}$, we consider all possible groups of images that observe P_k . Specifically, each group $\mathcal{G}_i = I_{\text{ref}_i}, I_{\text{src}_i^1}, I_{\text{src}_i^2}, I_{\text{src}_i^3}$ consists of one reference image and three corresponding source images. Our method involves the basic $W2C$ steps.

We project P_k onto the 2D image planes of each image $I_j \in \mathcal{G}_i$:

$$\begin{bmatrix} u_{k_j} \\ v_{k_j} \\ 1 \end{bmatrix} = \frac{1}{Z_c} \begin{bmatrix} f_{x_j} & 0 & c_{x_j} & 0 \\ 0 & f_{y_j} & c_{y_j} & 0 \\ 0 & 0 & 1 & 0 \end{bmatrix} \begin{bmatrix} R_j & t_j \\ 0^T & 1 \end{bmatrix} \begin{bmatrix} X_{k_j} \\ Y_{k_j} \\ Z_{k_j} \\ 1 \end{bmatrix} \quad (9)$$

where (u_{k_j}, v_{k_j}) are the normalized pixel coordinates of I_j , f_{x_j} and f_{y_j} are the focal lengths of camera I_j along the x

and y axes, respectively. c_{x_j} and c_{y_j} are the image center coordinates. $R_j \in SO(3)$ and t_j are the rotation matrix and translation vector of I_j respectively. We then compute the Euclidean distance between the projected point (u_{k_j}, v_{k_j}) and the principal point (image center) (c_{x_j}, c_{y_j}) of image I_j :

$$d_{k_j} = \sqrt{(u_{k_j} - c_{x_j})^2 + (v_{k_j} - c_{y_j})^2}. \quad (10)$$

For each image group \mathcal{G}_i observing P_k , we calculate the average Euclidean distance:

$$D_{\text{avg}}(P_k, \mathcal{G}_i) = \frac{1}{|\mathcal{G}_i|} \sum_{I_j \in \mathcal{G}_i} d_{k_j} \quad (11)$$

Among all possible four-image groups that observe P_k , we select the group with the smallest $D_{\text{avg}}(P_k)_{\min}$. This ensures that P_k is primarily reconstructed using images where it is closest to the image centers in their respective 2D planes, thereby enhancing the reliability of its triangulation. Since we want to select the optimal image group for every initial SfM point in the sub-regions. We simply identify the group for P_k \mathcal{G} by minimizing D_{avg} :

$$\mathcal{G}_{\text{opt}}(P_k) = \underset{\mathcal{G}_i}{\text{agr min}} D_{\text{avg}}(P_k, \mathcal{G}_i). \quad (12)$$

This ensures that P_k is reconstructed using images where it appears closest to the image centers, enhancing reconstruction reliability due to reduced distortion and higher image quality near the center. After determining $\mathcal{G}_{\text{opt}}(P_k)$ for all points $P_k \in \mathcal{P}$, we aggregate the utilized images I_{used} and exclude any images not present:

$$I_{\text{used}} = \bigcup_{P_k \in \mathcal{P}} \mathcal{G}_{\text{opt}}(P_k) \quad (13)$$

After determining the best image groups for all 3D points within the sub-region, we exclude any images that do not appear in any of the selected best groups. In our experiments, the excluded images are mainly located at the outermost sides of the sub-region, which means they are redundant images which can only observe a few points in the region.

Table 1
Example Per Scene Partitioning Strategy.

Scene	Images	Grid Size	Used
Campus [35]	5871	8×8	41
Residence [35]	2582	6×6	20
SZTU [54]	1500	6×6	17
LOWER_CAMP [54]	670	4×4	12

4.1.5. Scene Partitioning Strategy

To address the issue where some sub-regions may contain too few points (especially in boundary areas) after dividing the scene into smaller parts, we evaluate each sub-region as follows: We retain a sub-region only if both the number of points and the number of matched images within it reach at least 10 % of the average per-subregion counts (i.e., the total number of points or images divided by n^2).

We partition each scene based on the number of images to ensure efficient processing and optimal reconstruction quality. Specifically, we divide the regions according to the following criteria:

1. Scenes with fewer than 1,000 images are divided into a 4×4 grid.
2. Scenes with fewer than 3,000 images are divided into a 6×6 grid.
3. Scenes with more than 3,000 images are divided into an 8×8 grid.

Table 1 lists the examples of the number of initially partitioned sub-regions for each scene and the number of sub-regions that were ultimately included in the training after applying our filtering criteria based on point cloud density and image coverage.

4.2. Adaptive Multi-View Densification

In this section, we detail how multi-view geometric consistency is exploited to introduce densification based on rendered depth maps for 2DGS. As demonstrated in Figure 1 (Stage 2), each subregion can be assigned to an independent GPU for training. However, vanilla 2DGS often struggles to capture fine geometry details due to densification based on single-view image gradients, resulting in low-fidelity rendering and overly smooth geometry extraction. Therefore, it is necessary to add more fine Gaussian primitives for capturing high-frequency geometric details [13, 27, 10, 66]. In ULSR-GS, we perform additional densification via an MVS-like approach to address the limitations of overly smooth meshes resulting from D_{mean} computations in Eq. 3 from TSDF fusion. This method projects D_{mean} into 3D space [61, 11] and combines it with the RGB information of the GT image to enrich the Gaussian primitives.

4.2.1. Multi-view depth aggregation.

In our approach, we perform weighted averaging of depth from multiple source views. This weighting assigns a confidence score to each depth estimate based on its geometric consistency [61], ensuring that source views with

higher consistency have a greater influence on the final depth estimation.

Since we have 3 source views from Eq. (8), with each rendered depth D_{mean} denoted as \mathbf{D}_{src_i} for $i = 1, 2, 3$, and the depth map of the reference view denoted as \mathbf{D}_{ref} . For each pixel p_{ref} in the reference view, the final fused depth estimate $\mathbf{D}_{final}(p_{ref})$ is obtained through weighted fusion of the source views:

$$\mathbf{D}_{final}(p_{ref}) = \frac{\sum_{i=1}^N w_{src_i}(p_{src_i}) \cdot \mathbf{D}_{src_i}(p_{src_i})}{\sum_{i=1}^N w_{src_i}(p_{src_i})}, \quad (14)$$

where $\mathbf{D}_{src_i}(p_{src_i})$ is the depth value at the projected pixel p_{src_i} in the i -th source view corresponding to p_{ref} . The weight $w_{src_i}(p_{src_i})$ is based on the geometric consistency score, measuring the reliability of the depth estimate from the i -th source view:

$$w_{src_i}(p_{src_i}) = \exp\left(-\frac{E_{depth}(p_{ref}, p_{src_i})}{\sigma^2}\right), \quad (15)$$

where $E_{depth}(\cdot)$ represents the depth error between the reference view and the source view:

$$E_{depth}(p_{ref}, p_{src_i}) = \left| \mathbf{D}_{ref}(p_{ref}) - \mathbf{D}_{src_i}(p_{src_i}) \right| \quad (16)$$

4.2.2. Adaptive depth densification.

Directly projecting all depth as new 2D Gaussian primitives after checking the geometric consistency introduces excessive redundant information into the training scene [27]. This redundancy negatively impacts both the training speed and the accuracy of the scene representation. To address this issue, we introduce an adaptive densification window mask that confines the densification area. This approach eliminates inaccurate values at the edges of the depth map and adaptively accounts for non-uniform depth changes caused by varying viewpoint poses.

To determine the mask size adaptively, we base it on the depth gradient $|\nabla \mathbf{D}(x)|$, which represents the rate of change in depth at each pixel x . The window size is inversely proportional to the mean gradient \bar{g} , implying that regions with higher depth variations have smaller windows to capture finer details, while regions with lower variations have larger windows. We first compute the mean gradient \bar{g} over the entire depth map of size $h \times w$:

$$\bar{g} = \frac{1}{h \times w} \sum_{x \in \mathbb{D}} |\nabla \mathbf{D}(x)| \quad (17)$$

Based on the average gradient \bar{g} , we define the height and width of the window to dynamically adapt to the depth changes in the scene:

$$(h_{win}, w_{win}) = \frac{k}{\bar{g} + \epsilon} \cdot \frac{(h, w)}{2} \quad (18)$$

where k and ϵ are proportional constants that control the change in window size. The term ϵ prevents division by zero when the gradient is very small.

Table 2

Quantitative results on GauU-Scene dataset [54]. We report precision, recall, and F-1 score at the threshold $\tau = 0.025$ (relative). The **best** and second results are highlighted. "OOM" denotes no results due to GPU out of memory. "*" denotes no result due to no convergence.

Scene	LOWER_CAMP			UPPER_CAMP			LFLS			SMBU			SZIT			SZTU			
Metrics ($\tau = 0.025$)	Pre. \uparrow	Rec. \uparrow	F1 \uparrow	Pre. \uparrow	Rec. \uparrow	F1 \uparrow	Pre. \uparrow	Rec. \uparrow	F1 \uparrow	Pre. \uparrow	Rec. \uparrow	F1 \uparrow	Pre. \uparrow	Rec. \uparrow	F1 \uparrow	Pre. \uparrow	Rec. \uparrow	F1 \uparrow	Time
Neuralangelo	*	*	*	*	*	*	*	*	*	*	*	*	*	*	*	*	*	*	>100 h
SuGaR	0.279	0.263	0.271	0.261	0.273	0.267	0.271	0.300	0.285	0.376	0.409	0.392	0.249	0.276	0.263	0.272	0.299	0.285	4.1h
2DGS-60K	0.583	0.693	0.633	0.554	0.563	0.559	0.543	0.557	0.550	0.580	0.745	0.652	0.584	0.617	0.600	<u>0.596</u>	<u>0.613</u>	<u>0.604</u>	2.1h
GOF-60K	0.667	0.652	0.659	0.693	0.672	<u>0.682</u>	<u>0.607</u>	<u>0.659</u>	<u>0.631</u>	<u>0.679</u>	0.784	<u>0.727</u>	0.649	<u>0.695</u>	<u>0.671</u>	OOM	OOM	OOM	5.3h
PGRS-60K	0.683	0.648	<u>0.665</u>	0.672	<u>0.673</u>	0.672	OOM	OOM	OOM	0.660	0.795	0.721	<u>0.679</u>	0.642	0.659	0.548	0.542	0.545	5.7h
Ours	<u>0.681</u>	<u>0.689</u>	0.685	<u>0.690</u>	0.705	0.697	0.684	0.703	0.693	0.737	<u>0.789</u>	0.762	0.705	0.713	0.709	0.713	0.723	0.718	<u>3.7h</u>

Table 3

Quantitative results on Matrix City dataset (Small City Scene) [25] and two custom-collected datasets (Scene1 and Scene2). We report precision, recall, and F-1 score at different distance thresholds $\tau = 1.0m$ and $\tau = 0.5m$ (metric). The **best**, second results are highlighted. "OOM" denotes no results due to GPU out of memory. Note that "City-GS V2+Ours(2x2)" means we train CityGaussianV2 [34] on our proposed partition method.

Metrics	Matrix City						Scene1						Scene2					
	$\tau = 1.0m$			$\tau = 0.5m$			$\tau = 1.0m$			$\tau = 0.5m$			$\tau = 1.0m$			$\tau = 0.5m$		
	Pre. \uparrow	Rec. \uparrow	F1 \uparrow	Pre. \uparrow	Rec. \uparrow	F1 \uparrow	Pre. \uparrow	Rec. \uparrow	F1 \uparrow	Pre. \uparrow	Rec. \uparrow	F1 \uparrow	Pre. \uparrow	Rec. \uparrow	F1 \uparrow	Pre. \uparrow	Rec. \uparrow	F1 \uparrow
2DGS-60K (Baseline)	0.551	0.692	0.613	0.331	0.502	0.398	OOM	OOM	OOM									
City-GS V2	0.871	<u>0.901</u>	<u>0.886</u>	0.667	<u>0.753</u>	0.707	OOM	OOM	OOM									
City-GS V2+Ours(2x2)	-	-	-	-	-	-	0.845	<u>0.875</u>	<u>0.860</u>	0.646	<u>0.753</u>	<u>0.695</u>	<u>0.702</u>	<u>0.746</u>	<u>0.723</u>	0.569	<u>0.637</u>	<u>0.601</u>
Ours	<u>0.869</u>	0.916	0.892	<u>0.660</u>	0.759	<u>0.706</u>	<u>0.837</u>	0.929	0.880	<u>0.632</u>	0.787	0.701	0.710	0.748	0.728	0.569	0.651	0.607

We then project the depth $\mathbf{D}_{\text{final}}$ within the window $W(u, v) \in (h_{\text{win}}, w_{\text{win}})$ after the geometric consistency check and fusion from Eq. (14):

$$\mathbf{P}_w(u, v) = \mathbf{D}_w(u, v) \cdot \mathbf{K}_p^{-1} \begin{bmatrix} u \\ v \\ 1 \end{bmatrix} \quad (19)$$

where \mathbf{K}_p^{-1} is the inverse of the intrinsic camera matrix, and $\mathbf{P}_w(u, v)$ represents the 3D point projected from the windowed depth map. Following the settings of MVG-Splatting [27], we perform additional rescaling and rotational alignment on the newly added Gaussian primitives after each densification step to ensure consistency across the scene.

4.3. Loss Functions

Geometric consistency loss. We optimize the geometric consistency between the reference view and the source views via the *reprojection error* that compares the reprojected reference depth \mathbf{D}_{ref} with the source depth \mathbf{D}_{src} in the source view as defined in Eq. (16).

Multi-view normal consistency loss. For each projected point, we compute the angular error between the normal vectors of the reference view \mathbf{N}_{ref} and the source view \mathbf{N}_{src} . This normal vector consistency ensures that the geometry of the primitive remains consistent under different viewing angles:

$$E_{\text{normal}} = 1 - \frac{\mathbf{N}_{\text{ref}} \cdot \mathbf{N}_{\text{src}}}{\|\mathbf{N}_{\text{ref}}\| \|\mathbf{N}_{\text{src}}\|} \quad (20)$$

Final loss function. The final loss function is defined as:

$$L = \alpha \cdot E_{\text{depth}} + \beta \cdot E_{\text{normal}} + L_{\text{geo}} + L_r \quad (21)$$

where α, β , are weighting factors that balance the contributions of each error term. $L_{2\text{DGS}}$ includes two regularization components from 2DGS [16]: depth distortion ℓ_d and normal consistency ℓ_n . $L_{3\text{DGS}}$ represents the RGB reconstruction loss, combining L_1 loss and the D-SSIM metric as used in 3DGS [19].

5. Experiments

5.1. Implementation

In our experiments, we initially employ COLMAP [44] to obtain the SfM results for the entire scene. Subsequently, we align the sparse point cloud using the Manhattan World Alignment, ensuring that the y -axis is perpendicular to the xz plane. We set the angular threshold $\theta_{\text{min}} = 90$, and the distance threshold $D_{\text{max}} = \sqrt{d_x \times d_y}$, where d_x and d_y are the distances of each sub-region. After partitioning, we double the boundary of the initial point cloud for each region for the initialization. This configuration ensures that the edges of each subregion receive sufficient training information, thereby preventing edge mismatches during the stitching process. Redundant points are automatically pruned during training through opacity culling. Experiments for our method are conducted on 4 RTX 4090 GPUs, and each sub-region is trained individually by one GPU.

For each subregion, training is conducted for 40k iterations. Adaptive multi-view densification begins at the 20k-th iteration and terminates at the 30k-th iteration. Regarding the loss function, we set the parameters $\alpha = 0.01$ and $\beta = 0.1$. All other loss functions and training parameters are configured identically to those used in 3DGS and 2DGS frameworks. After training, we employ TSDF [50] to extract the mesh of each sub-region then crop using their partition bounding boxes and subsequently stitched together.

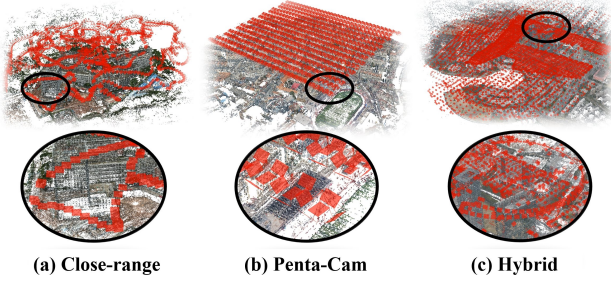


Figure 3: Examples of experiment datasets. Our experiments are conducted on different types of aerial oblique photography datasets, such as (a) close-range photogrammetry, (b) five-directional (penta-cam) photogrammetry, and (c) hybrid photogrammetry which contains both close-range and penta-cam photogrammetry.

5.2. Datasets

As shown in Figure 3, our experiments are conducted on large-scale aerial oblique photogrammetry datasets: GauU-Scene (GauU) [54], UrbanScene3D (US3D) [35], and two custom-collected datasets, namely Scene 1 and Scene 2 (example rendering results can be found at Figure 5). Both Scene 1 (Penta-Cam) and Scene 2 (Close-range + Penta-Cam) contain around 10,000 images.

1. GauU-Scene (GauU) [54] dataset is a large-scale dataset specifically for Gaussian Splatting. It contains six areas with an average coverage of more than 1 km^2 . However, each scene only contains an average of 1,200 high-resolution drone oblique photography images with an average overlap rate of no more than 50%. The lack of densification caused by sparse data will cause serious under-reconstruction, which poses a great challenge to the single-GUP-based GS modeling. We use the UAV-scanned LiDAR point cloud provided by GauU as the ground truth (GT) for the evaluation mesh.
2. UrbanScene3D (US3D) [35] dataset is a large-scale urban dataset that is strictly collected according to the requirements of oblique photography. The ‘Campus’ scene contains 5,000 Penta-Cam images within 2.5 km, with an overlap rate of more than 70%, which is a great challenge for the GS method with a single GPU, and also for the training strategy of multiple GPUs. It also contains two close-range oblique photogrammetry scenes, which poses a challenge to the partitioning strategy of the GS method with multiple GPUs.

3. We also include two additional custom-collected datasets in the real world. Scene 1 has a measurement range of about 4 km^2 , and uses Penta-Cam to collect more than 8,000 high-resolution complete campus images. Scene 2 is a 2 km^2 complex urban oblique photography dataset containing a large amount of water environment and skyscrapers. It uses Penta-Cam for overall collection, combined with close-range shooting to take separate supplementary photos of each skyscraper over 200 m. This uneven collection of 10,000 images is very close to the actual photogrammetry collection process, which poses a great challenge to all GS methods. We also use USV orthophoto LiDAR scanning to collect point clouds within the coverage area as ground truth.

5.3. Metrics

For evaluating NVS rendering results, we employ PSNR, SSIM, and LPIPS on Urbanscene3D and GauU datasets. In assessing the reconstructed meshes, we report Precision, Recall, and F-score against the GT Lidar pointclouds on GauU-scene dataset, and two custom collected Scene1, and Scene2. Following the settings of Vast Gaussian [29], we adjust the training configurations for all GS-based methods for a fair comparison. The input training photos are downsampled by a factor of 4 (except for the Matrix City dataset [25]).

5.3.1. Rendering quality evaluation

- PSNR (Peak Signal-to-Noise Ratio): Measures the pixel-wise difference between the rendered images and the ground truth images:

$$\text{PSNR} = 10 \cdot \log_{10} \left(\frac{\text{MAX}_I^2}{\text{MSE}} \right) \quad (22)$$

where MAX_I is the maximum possible pixel value and MSE is the Mean Squared Error.

- SSIM (Structural Similarity Index Measure): Evaluates perceived image quality based on luminance, contrast, and structure:

$$\text{SSIM}(x, y) = \frac{(2\mu_x\mu_y + C_1)(2\sigma_{xy} + C_2)}{(\mu_x^2 + \mu_y^2 + C_1)(\sigma_x^2 + \sigma_y^2 + C_2)} \quad (23)$$

- LPIPS (Learned Perceptual Image Patch Similarity): Measures perceptual similarity by comparing features extracted from pretrained neural networks:

$$\text{LPIPS}(x, y) = \sum_l \frac{1}{H_l W_l} \sum_{h,w} \|w_l \odot (\hat{y}_l^{hw} - \hat{x}_l^{hw})\|_2^2 \quad (24)$$

5.3.2. Mesh quality evaluation

Since GauU-scene [54] does not provide a standard evaluation code, we follow the Tanks and Tample [21] evaluation pipeline to quantitatively assess reconstructed meshes against GT LiDAR point clouds:

Urban Scale Surface Reconstruction

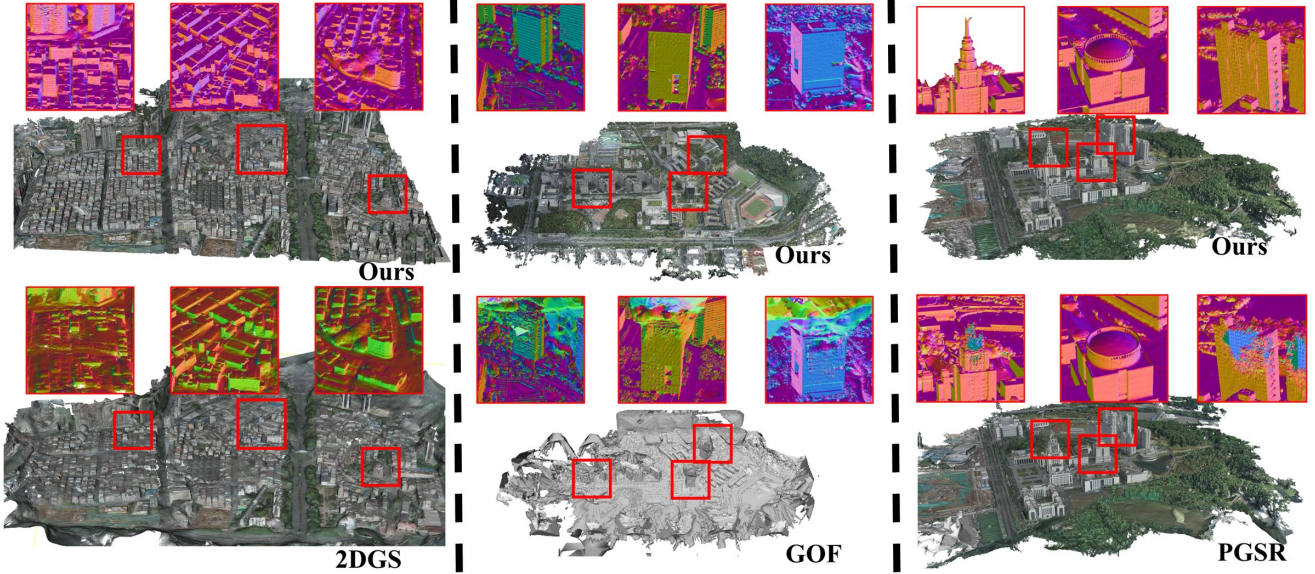


Figure 4: Qualitative comparison with single GPU GS-based methods. We show the full scene comparison with 2DGS [16], GOF[66], and PGSR[5]. From left to right are the *LFLS*, *SZIIT*, and *SMBU* scenes of the GauU-Scene [54] dataset.

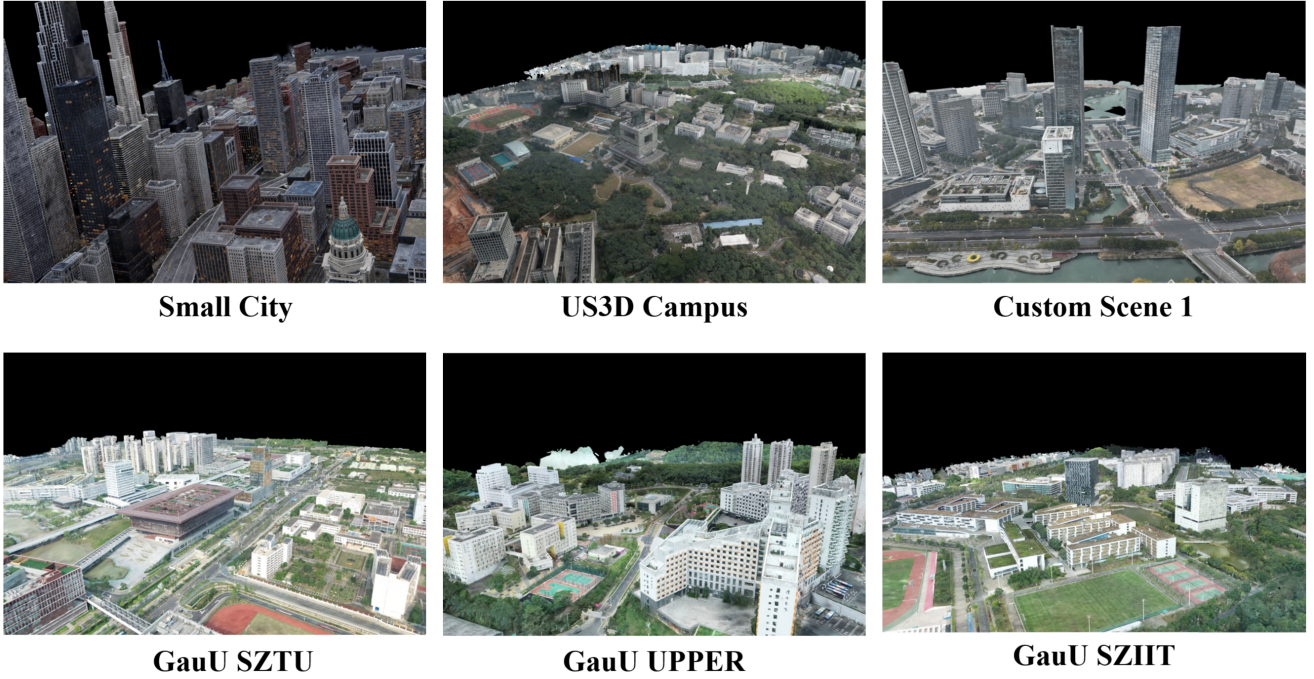


Figure 5: Rendering Results. We demonstrate the full-scene (zoomed-out) rendering detail of the selected scenes.

1. To focus the evaluation on relevant regions, we compute the overlapping axis-aligned bounding box of both point clouds and mesh and crop them accordingly. We then perform Iterative Closest Point [43] (ICP) alignment to minimize misalignment between the reconstructed and GT point clouds.
2. We uniformly sample number of points from the reconstructed mesh and GT points to 50 million.
3. We utilize *KDTreeFlann* to compute precision, recall, and F-score using predefined distance thresholds.

4. Precision (Pre): Evaluates the accuracy of reconstructed surfaces against ground truth:

$$\text{Precision} = \frac{|\{p \in \mathcal{P}_{\text{rec}} | d(p, \mathcal{P}_{\text{gt}}) < \tau\}|}{|\mathcal{P}_{\text{rec}}|} \quad (25)$$

5. Recall (Rec): Measures the completeness of reconstruction:

$$\text{Recall} = \frac{|\{p \in \mathcal{P}_{\text{gt}} | d(p, \mathcal{P}_{\text{rec}}) < \tau\}|}{|\mathcal{P}_{\text{gt}}|} \quad (26)$$

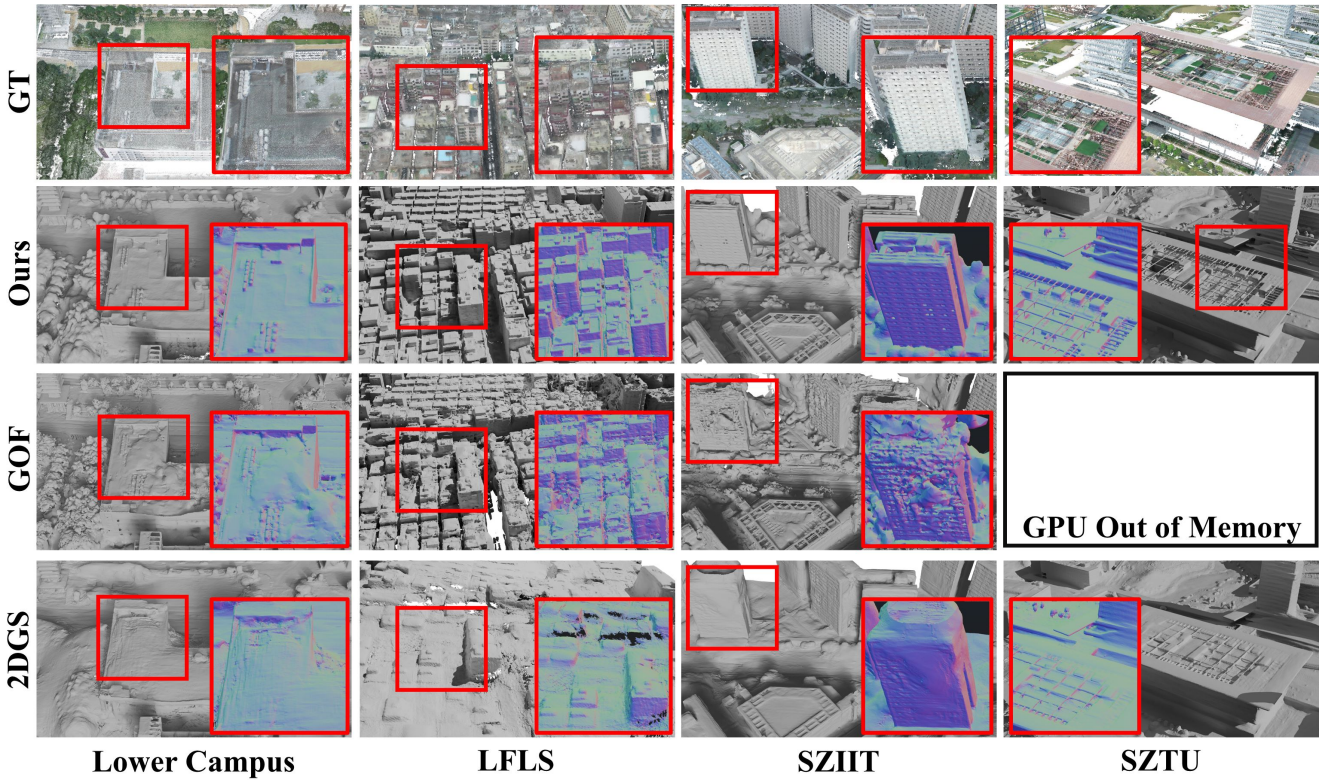


Figure 6: Qualitative comparison on the GauU-Scene dataset [54]. We demonstrate the zoomed-in surface normal detail of the selected areas in red box.

6. F-1 Score: Provides a balanced measure combining Precision and Recall:

$$F1 \text{ Score} = 2 \times \frac{\text{Precision} \times \text{Recall}}{\text{Precision} + \text{Recall}} \quad (27)$$

5.4. Compared methods.

We compare our proposed ULSR-GS with: (1) single-GPU-based GS methods capable of mesh extraction, including SuGaR [15], 2DGS [16], GOF [66], and PGSR [5]; (2) multi-GPU-based GS method capable of mesh extraction CityGaussianV2 [34]; (3) open source or free-to-use MVS-based photogrammetry projects, including COLMAP and Reality Capture; and (4) we also compare Vast Gaussian’s [29] partition strategy on rendering tasks and geometry task.

5.5. Experiment results.

5.5.1. Comparison with single-GPU-based GS Methods.

It is important to note that the comparison with single-GPU methods is only as fair as possible. We increase the training iterations of all single-GPU methods by a factor of 2 as much as possible on hardware with 24GB VRAM (a factor of 3 or more will cause most methods to GPU out-of-memory (OOM)), and all training parameters were adjusted accordingly. The full-scene results clearly indicate that our method achieves reconstructions with substantially greater detail and completeness than these baselines.

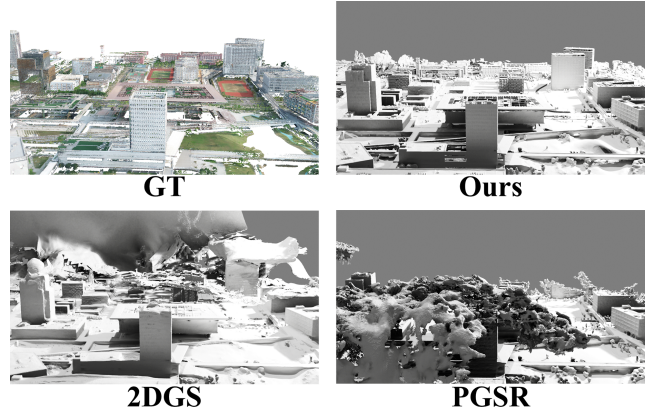


Figure 7: Qualitative comparison on the GauU-Scene [35] dataset *SZTU* scene. When the scene range expands and the number of images increases, the geometric reconstruction quality of 2DGS [16] and PGSR [5] drops sharply.

Figure 4 provides a qualitative comparison of ULSR-GS against three recent single-GPU reconstruction methods: 2DGS [16], GOF [66], and PGSR [5]. In particular, the 2DGS [16] approach produces excessively smooth mesh surfaces that fail to capture fine-grained architectural details, especially in densely built areas. As a result, it cannot accurately reconstruct the intricate geometry of building structures in such regions. The GOF [66] method, which

employs a marching tetrahedron algorithm for mesh extraction, often yields meshes with spurious connections to the sky. These artifacts disrupt the continuity of the model and prevent GOF from producing a correct, complete outline of the urban scene. Although PGSR [5] leverages multi-view geometric constraints similar to our method, it selects source views based on those closest in viewpoint to the reference image. In aerial oblique photography scenarios, this strategy frequently chooses source images whose content diverges significantly from the reference view’s observations, hindering effective multi-view geometric consistency enforcement. Consequently, as shown in Figure 7 PGSR’s reconstructions suffer from reduced mesh integrity and completeness. In contrast, our method avoids these issues and preserves both the fine details and the overall structural integrity of the reconstructed urban scene.

Table 2 presents a quantitative evaluation of reconstruction quality on the GauU-Scene dataset [54], using precision, recall, and F1-score metrics at the distance threshold $\tau = 0.025$. Our proposed approach demonstrates superior performance across all evaluated scenes, significantly outperforming other single GPU-based Gaussian Splatting (GS) methods in both precision and completeness metrics. Specifically, our method consistently achieves the highest or second-highest scores, reflecting robust reconstruction accuracy and completeness.

Regarding computational efficiency, our method, running on four GPUs, achieves shorter training times compared to single-GPU methods GOF [66] and PGSR [5] at 60K iterations. Notably, GOF and PGSR suffer from OOM issues in specific complex scenes due to their similar densification strategies, limiting their applicability for large-scale reconstructions. This clearly highlights the efficacy and scalability of our partitioning strategy, which effectively mitigates GPU memory limitations and enables comprehensive reconstruction even in resource-constrained environments. Furthermore, detailed qualitative visual comparisons in Figure 6 clearly illustrate the superior detail reconstruction capability of our method. The magnified detail results highlight significant improvements in geometric accuracy and fine detail representation compared to the baseline methods.

5.5.2. Comparison with multi-GPU-based GS Methods.

Table 3 presents a quantitative evaluation comparing our proposed method with existing multi-GPU-based GS methods on the Matrix City dataset [25], and two additional custom-collected datasets (Scene1 and Scene2). Precision, recall, and F1-scores are reported at two different distance thresholds ($\tau = 1.0m$ and $\tau = 0.5m$).

Our method consistently achieves the best or second-best results across metrics, underscoring the effectiveness and superiority of our per-point partitioning strategy in overcoming scalability bottlenecks, enabling efficient and accurate reconstruction of complex urban scenes. CityGaussianV2 [34], another multi-GPU-based method, similarly requires initial coarse training on a single GPU followed by

Table 4

Quantitative between MVS-based and GS-based Meshes. We report precision, recall, and F-1 score at distance threshold $\tau = 0.5m$. The **best**, **second** results are highlighted. "OOM" denotes no results due to VRAM/RAM out of memory during training or TSDF-fusion. "ds" denotes image down sample factor and "v" denotes voxel size. We also report the total time of obtion final mesh results (train + extraction).

Metrics	Pre.↑	Rec.↑	F1↑	Face (M)	Time (h) ↓
COLMAP (ds=4)	0.630	0.798	0.704	372.3	29.1
COLMAP (ds=1)	0.707	0.814	0.756	627.9	69.2
Reality Capture (ds=4)	0.629	0.794	0.702	335.6	17.7
Reality Capture (ds=1)	0.703	0.832	0.762	1021.2	61.4
2DGS (ds=4)	OOM	OOM	OOM	OOM	OOM
CityGSV2 (ds=4, v=0.4m)	0.646	0.753	0.695	<u>357.2</u>	16.1
CityGSV2 (ds=4, v=0.1m)	OOM	OOM	OOM	OOM	OOM
Ours (ds=4, v=0.4m)	0.632	0.787	0.701	335.6	<u>16.7</u>
Ours (ds=4, v=0.1m)	0.667	0.799	0.727	983.5	19.8

partitioning for multi-GPU fine-tuning. However, this training paradigm becomes infeasible for datasets comprising nearly 10,000 images, such as Scene1 and Scene2, where the initial sparse point cloud generated by COLMAP exceeds 30 million points, surpassing the memory limitations of a single RTX 4090 GPU with 24GB VRAM. To address this challenge, we applied our proposed per-point partitioning strategy, dividing these two extensive scenes into smaller, manageable 2x2 sub-regions to apply the standard CityGaussianV2 training strategy. Consequently, as shown in the Table 3, this adaptation significantly improves the performance of CityGaussianV2 on the larger scenes.

In the qualitative comparison shown in Figure 8, CityGaussianV2 generates meshes with relatively sharp edges; however, significant holes emerge in smooth and low-texture regions such as roads and ground surfaces, negatively impacting its recall metrics and consequently resulting in lower F1-scores. Additionally, reflective surfaces, such as building glass facades, are inadequately reconstructed by CityGaussianV2, leading to incomplete structural representations. In contrast, our method successfully achieves a balanced reconstruction in both geometric detail and completeness, consistently outperforming CityGaussianV2 in both qualitative visual comparisons and quantitative metrics.

5.5.3. Comparison with MVS-based Methods.

From Table 4, we compare our method against traditional MVS-based approaches (e.g., COLMAP, Reality Capture) and GS-based methods (e.g., 2DGS, CityGSV2). Our approach demonstrates notable advantages in terms of reconstruction efficiency, memory efficiency, and structural detail preservation. As shown in Table 4, our approach achieves a competitive F1 score (0.701 at ds=4, v=0.4m) while maintaining a significantly lower computational cost (16.7 hours) compared to MVS-based methods like Reality Capture, which requires ds=1 to achieve better detail (F1: 0.762, 61.4 hours). Qualitative results in Figure 9

Urban Scale Surface Reconstruction

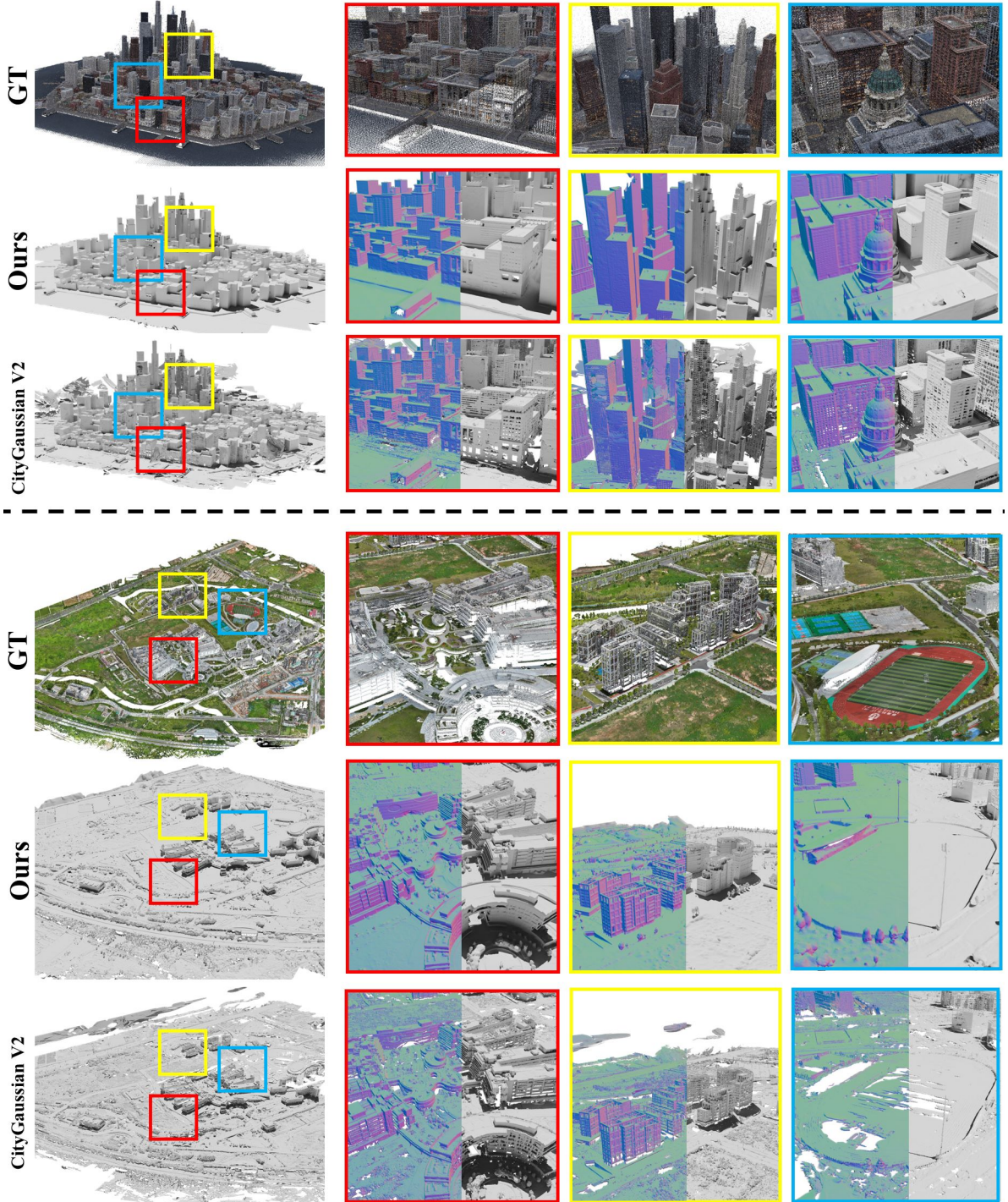


Figure 8: Qualitative comparison between ULSR-GS and CityGaussianV2 [34] on the Matrix City dataset [25] *Small City* scene and the custom collected dataset *Scene1*. Our method is superior to CityGaussianV2 [34] in terms of building integrity and detail preservation.

further illustrate that our method preserves fine structures, such as pipes and complex architectural elements, even at $ds=4$, whereas Reality Capture produces smoother, less detailed meshes. Additionally, recall visualizations in Figure 10 and 11 highlight that our approach generates detailed DSMs at $ds=4$, whereas MVS-based methods require $ds=1$

to achieve comparable results, leading to increased computational overhead. Unlike other GS-based methods that suffer from memory limitations at fine voxel resolutions ($v=0.1m$), our method remains computationally feasible while achieving a high F1 score. These results emphasize the efficiency of our approach in large-scale urban reconstruction, providing

Urban Scale Surface Reconstruction

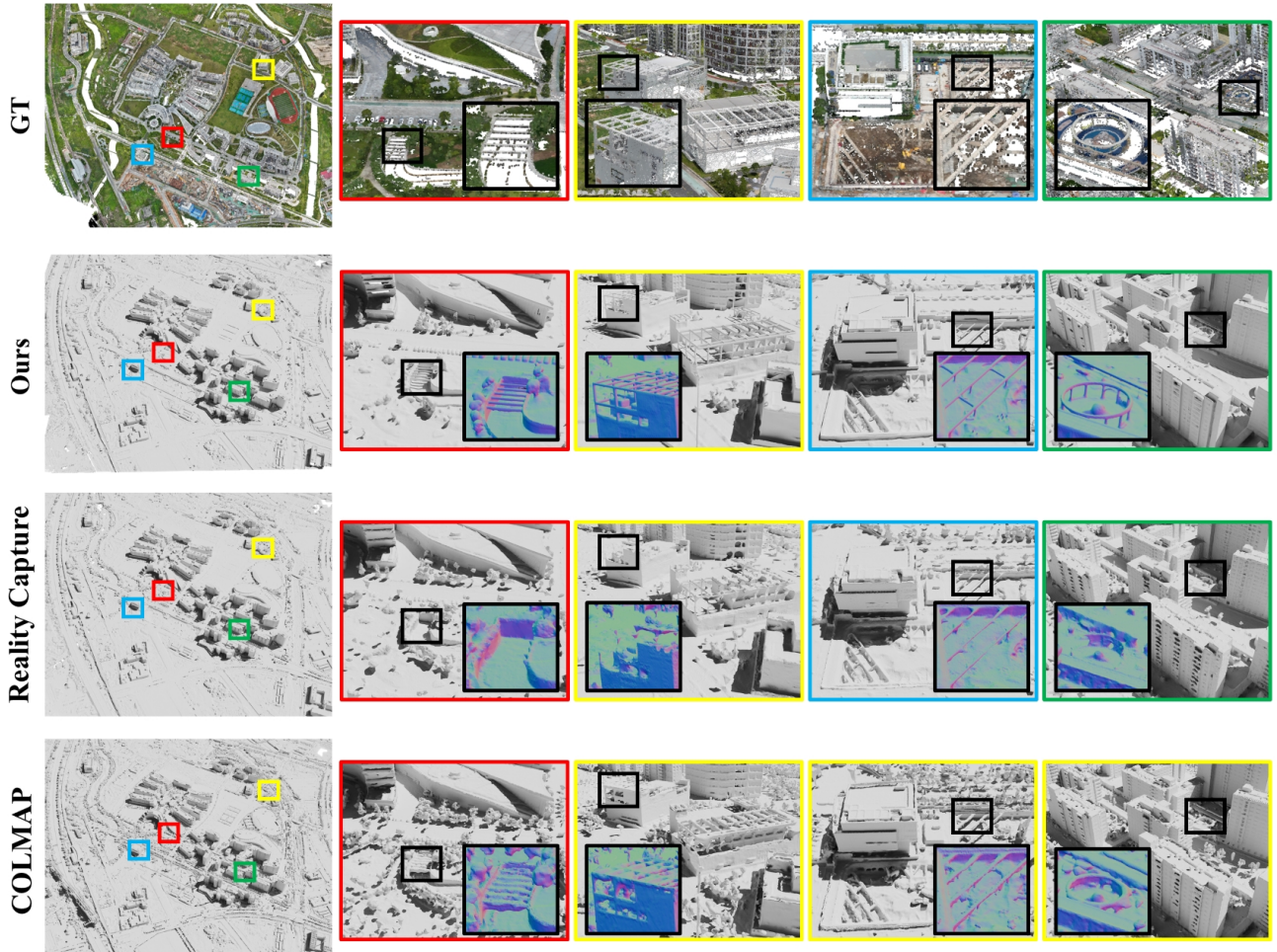


Figure 9: Qualitative comparison between ULSR-GS and Reality Capture and COLMAP on the custom collected dataset *Scene1*. We use a image downsampling factor of 4x on every method, and use the highest setting of Reality Capture and COLMAP for fair comparison. It can be seen that with the same downsampling factor, ULSR-GS can better reconstruct the thin geometric structure of the scene.

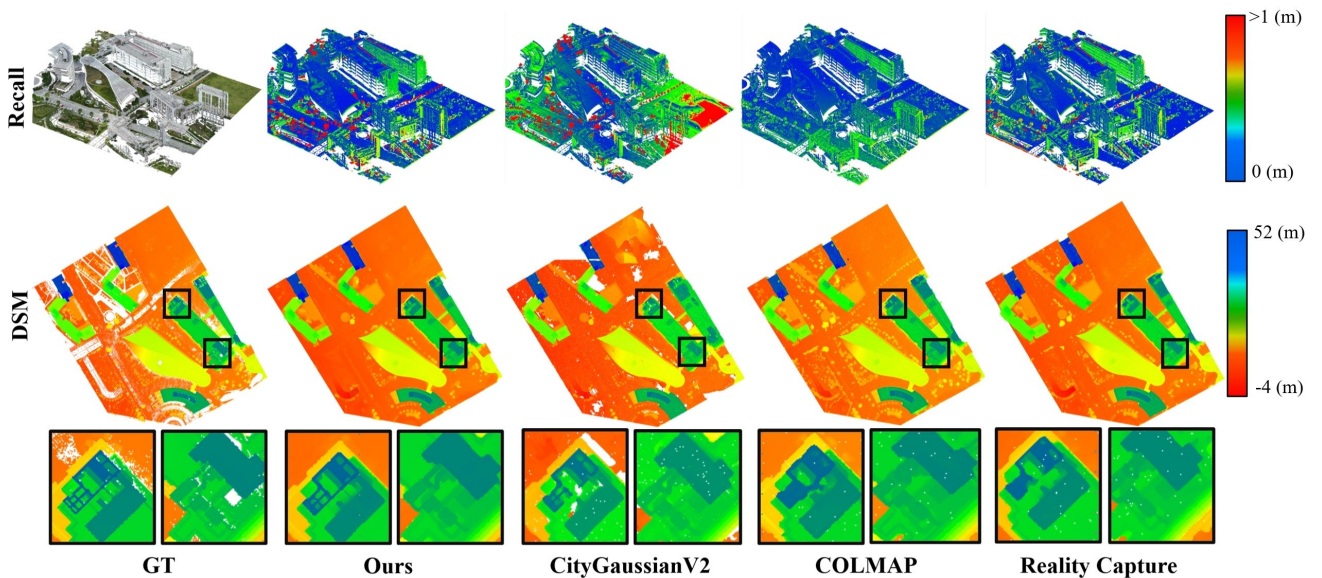


Figure 10: Qualitative evaluation of the Recall metric and the generated DSM.

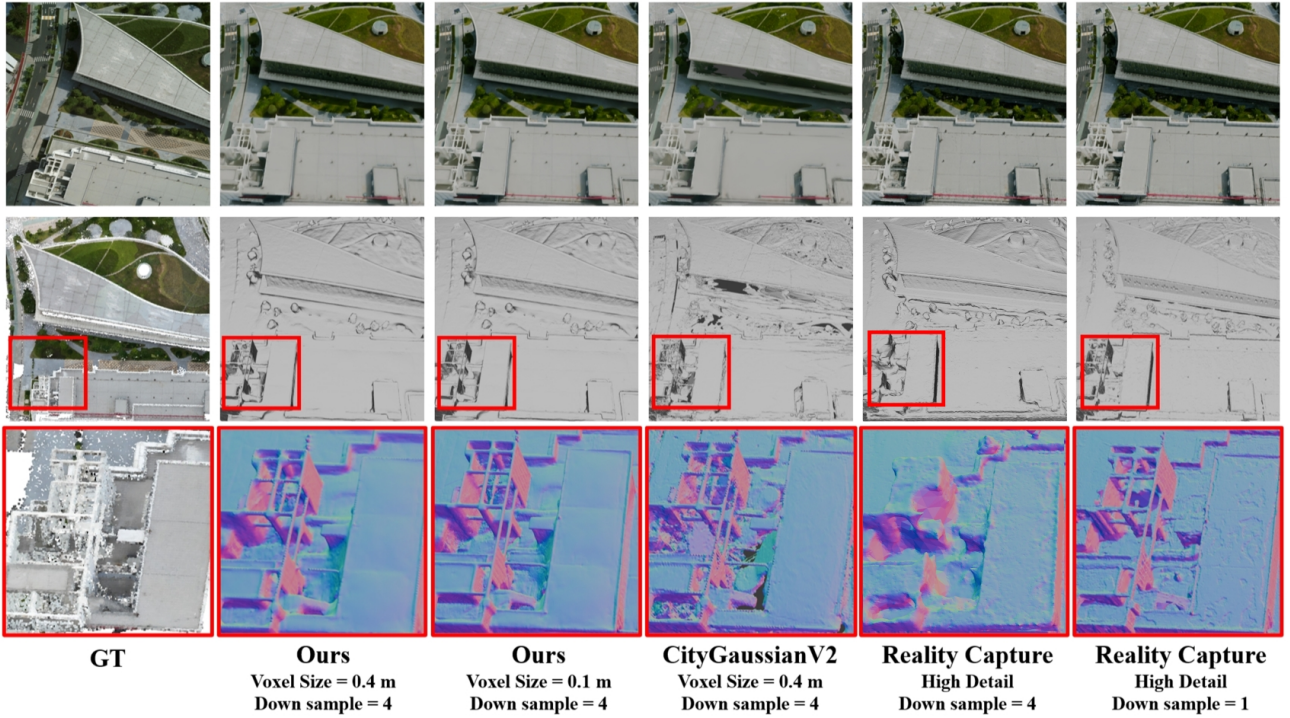


Figure 11: Qualitative evaluation of different parameter settings. From left to right: GT LiDAR, ULSR-GS with TSDF-fusion at 4x downsampling and 0.4m voxel size, ULSR-GS with TSDF-fusion at 4x downsampling and 0.1m voxel size, CityGaussianV2 with TSDF-fusion at 4x downsampling and 0.4m voxel size, RealityCapture with 4x downsampling and reconstruction quality set to "High Detail", and RealityCapture with 1x downsampling and reconstruction quality set to "High Detail".

Table 5
Geometric Consistency Constraints Ablation Studies. We conduct ablation experiments on the GauU-Scene dataset [54] in 4x4 cells. We reported metrics including Precision, Recall, F-1 Score. "-" denotes no data due to GPU out of memory.

	Precision. \uparrow	Recall. \uparrow	F-1 Score \uparrow
A. w/o E_{depth} & E_{normal}	0.659	0.661	0.660
B. w/o E_{depth}	0.663	0.665	0.664
C. w/o E_{normal}	0.652	0.651	0.651
D. w/o density	0.678	0.685	0.682
E. w density & w/o window mask	-	-	-
F. Full	0.681	0.689	0.685

high-quality 3D meshes with reduced processing time and memory requirements.

5.6. Ablation Study.

Table 5 presents the results of our ablation experiments, which quantitatively demonstrate the impact of removing geometric consistency constraints on reconstruction quality. Specifically, we observe that the absence of these constraints leads to a notable decline in Precision, Recall, and F1 Score, indicating that geometric consistency is essential for both accuracy and completeness.

5.6.1. Impact of Removing Individual Constraints

When both multi-view depth and normal consistency constraints are removed, it exhibits a noticeable performance decline, reinforcing the importance of geometric constraints

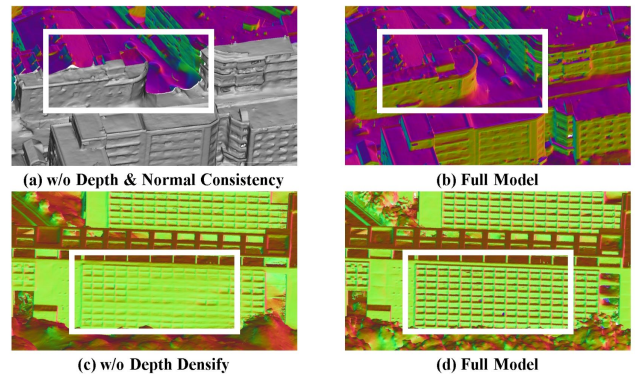


Figure 12: Qualitative comparison on the geometric consistency constraints ablation studies. Without E_{depth} & E_{normal} edges of each region fail to stitch seamlessly; Without adaptive density results in excessively smooth mesh extraction outcomes.

in high-quality reconstruction. Interestingly, the F1 score for this condition is slightly higher than that of removing normal consistency alone (Condition C). This suggests that when only normal consistency is absent, the retained depth consistency may introduce conflicting geometric that worsen reconstruction errors, whereas removing both constraints forces the model to rely solely on single image-based information, leading to a different but somewhat more stable degradation. Figure 12 (a) and (b) further highlights the

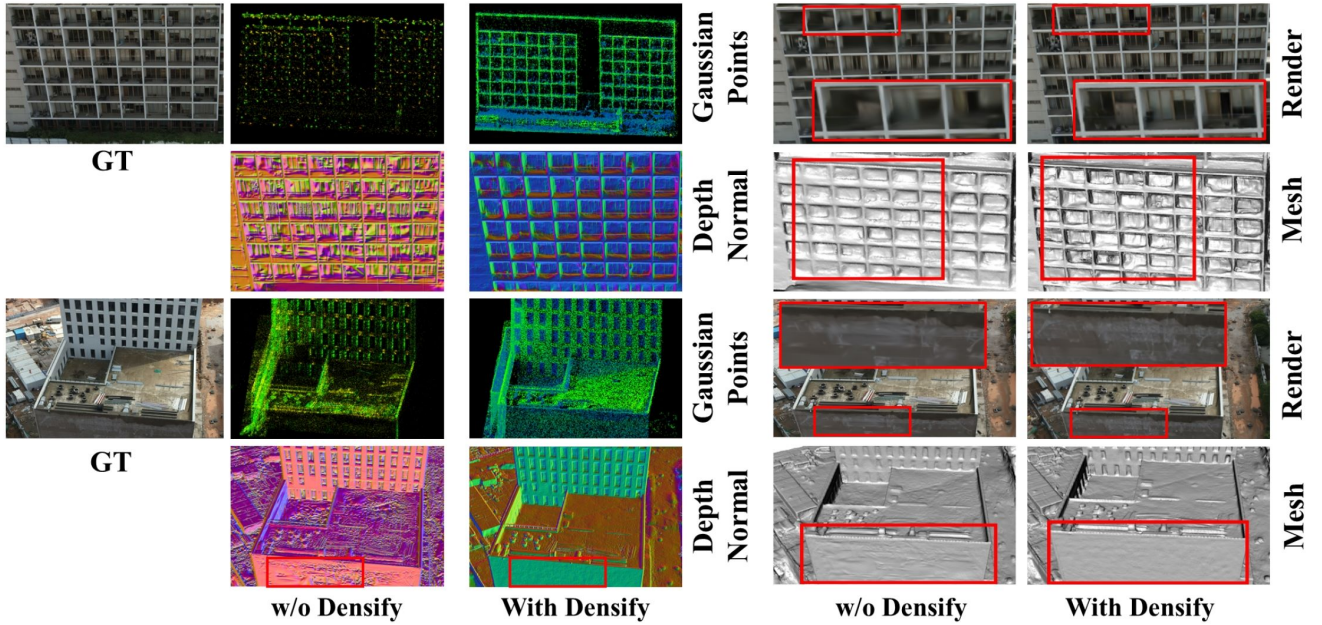


Figure 13: Qualitative comparison on the adapted depth densification ablation studies. Without adaptive densification (e.g. vanilla 2dgs gradient-based densification) results in excessively smooth mesh extraction outcomes and loss rendering quality.

dominant role of multi-view depth and normal consistency in preventing surface misalignment and ensuring smooth reconstructions.

When only the multi-view depth consistency is removed while retaining normal consistency, the moderate decline in performance suggests that although the absence of depth consistency introduces minor geometric misalignment across views, the retained normal consistency still preserves local surface smoothness and alignment, preventing a severe degradation in quality. This result implies that while depth consistency helps refine the global structure, normal consistency alone can still enforce a degree of geometric regularization, maintaining an acceptable level of reconstruction fidelity. When multi-view normal consistency is removed but depth consistency is retained, we observe a substantial drop in performance. This suggests that normal consistency plays a more critical role in maintaining surface quality than depth consistency alone. Without normal consistency, individual surfaces reconstructed from different views may exhibit inconsistent orientations, leading to visible artifacts, non-smooth transitions, and misaligned surface patches.

5.6.2. Impact of Densification Strategies.

When the densification process is removed, Precision and Recall drop slightly to 0.678 and 0.685, respectively, with an F1 Score of 0.682. However, the qualitative comparison in Figure 12 and 13 suggests that densification primarily refines the reconstruction rather than fundamentally altering its structure. The results indicate that while densification improves point distribution and mesh completeness, the geometric consistency constraints (depth and normal consistency) have a more significant impact on the overall

reconstruction quality. When remove window mask, ULSR-GS runs out of memory (OOM), preventing evaluation. This suggests that removing the window mask leads to an excessive increase in Gaussian points, which significantly inflates the computational burden. The failure to complete the reconstruction in this setting highlights the importance of an adaptive sparsification mechanism, which prevents unnecessary computational overhead while preserving reconstruction quality.

5.6.3. Impact of Partition Strategies

(a) Geometry Reconstruction

Table 6 presents comprehensive comparative experiments analyzing different partitioning strategies. In the absence of optimized pair selection (as demonstrated in Table 6(A)), a significant number of redundant images are included in training for each region. This redundancy not only substantially increases computational overhead but also negatively impacts the quality and precision of the extracted meshes. These redundant images typically originate from inaccuracies inherent to SfM computations [44], which fail to effectively filter images based solely on geometric consistency.

To further illustrate the robustness and effectiveness of our proposed partitioning strategy, we conducted experiments comparing our strategy against the image location-based partitioning method employed by Vast Gaussian [29]. Specifically, we evaluated both ULSR-GS and the baseline method 2DGS [16] under different partitioning conditions (Table 6(B), (C), and (D)). Our results demonstrate a clear superiority of our method, particularly in large-scale surface reconstruction scenarios.

Urban Scale Surface Reconstruction

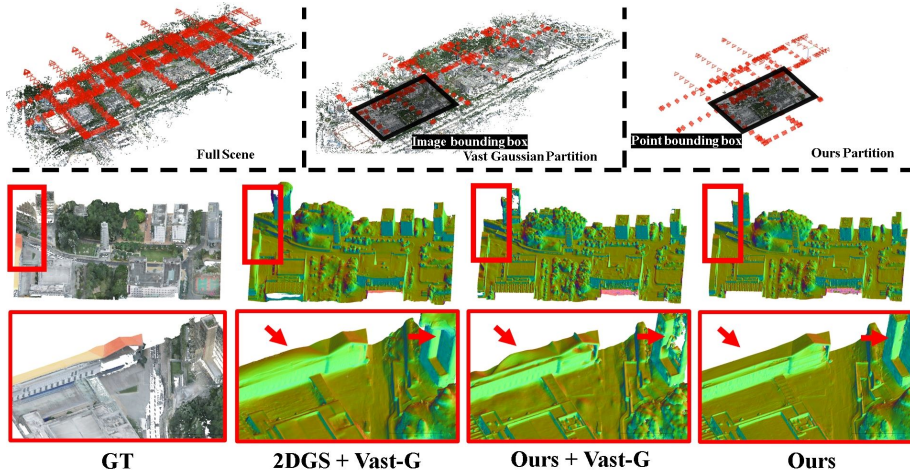


Figure 14: Qualitative comparison of partition strategies on a penta-cam dataset. The *black* bounding box is the same partition area. The image partition boundary for VastGaussian and the point cloud partition boundary for ULSR-GS are set to the same size according to the black boundary. Below are the meshes after clipping to the box size.

Notably, Figure 15 visually illustrates the effectiveness of our partitioning strategy using a more challenging close-range oblique photogrammetry dataset featuring intricate and specific UAV flight paths [35]. In this dataset, our approach successfully identifies and selects images highly relevant to the reconstruction region, significantly enhancing local detail preservation and accuracy. Conversely, the partitioning strategy of Vast Gaussian, which relies strictly on the projection of camera positions onto a 2D plane, selects images from a broader area without adequate precision. Consequently, critical images positioned outside of a predefined boundary, yet crucial for reconstructing complex structures, are erroneously excluded. Simultaneously, the inclusion of unrelated, distant images introduces noise, ultimately deteriorating the reconstruction quality. Additionally, on datasets collected using multi-directional Penta Cam setups in Figure 14, where camera paths and orientations are highly irregular, our point-to-photo partitioning approach consistently outperforms the camera projection-based method.

(b) Novel view synthesis.

Table 7 quantitatively compares different partitioning methods, specifically our point-based partitioning approach and the image-based method employed by Vast Gaussian [29]. The results indicate that the Vast Gaussian partitioning strategy is more suitable for rendering tasks. This is because our method prioritizes the reconstruction of the scene’s primary structure by excluding the distant sparse SfM points during sub-region partitioning. Figure 16 provides a qualitative comparison to further illustrate this difference. When training ULSR-GS using different partitioning strategies, our partition method shows a trade-off: while it loses performance in reconstructing the background, it preserves significantly more detail in the reconstruction of the primary scene components.

Table 6

Partition Strategies Comparison. We conduct experiments on the GauU-Scene dataset [54] scene in 4×4 cells. We reported metrics including Precision, Recall, and F-1 Score, Average number of images per cell, and Total training time. VastG[†] means the unofficial reproduction partition method of Vast Gaussian [29].

GauU-Scene (Avg. images: 957)	Pre. ↑	Rec. ↑	F1 ↑	Avg. I.	Time ↓
A. Ours w/o View Selection	0.699	0.707	0.702	437	4.5 h
B. Ours + Vast-G [†]	0.685	0.700	0.692	359	3.5 h
C. 2DGS + Ours	0.677	0.671	0.674	366	3.0 h
D. 2DGS + Vast-G [†]	0.663	0.669	0.667	359	2.9 h
E. 2DGS-60K (1 GPU)	0.573	0.631	0.600	957	2.1 h
F. ULSR-GS (4 GPU)	0.713	0.725	0.717	366	3.7 h

Data Type	Five-directional			Close-range					
	Scene	CUHK_LOWER [54]	Artsci [35]	Polytec [35]	Scene	CUHK_LOWER [54]	Artsci [35]	Polytec [35]	
Metrics	PSNR↑	SSIM↑	LPIPS↓	PSNR↑	SSIM↑	LPIPS↓	PSNR↑	SSIM↑	LPIPS↓
2DGS	23.85	0.711	0.382	25.42	0.763	0.346	24.96	0.849	0.236
2DGS+Vast-G	<u>24.98</u>	0.801	0.247	26.98	0.845	0.299	26.31	0.860	0.221
2DGS+Ours Partition	24.87	0.789	0.250	26.72	0.826	0.312	26.02	0.855	0.229
Ours+Vast-G	25.21	<u>0.805</u>	0.234	27.14	0.883	0.280	27.11	0.869	0.207
Ours	25.21	0.810	<u>0.239</u>	<u>27.01</u>	<u>0.851</u>	<u>0.289</u>	<u>26.97</u>	<u>0.861</u>	<u>0.213</u>

Table 7

Additional partition comparison. We conduct comparative experiments on different types of oblique photography datasets. Our partition strategy overemphasizes the reconstruction of the main area and deletes the background area with only a few reconstructed images, resulting in a decrease in the overall rendering quality.

Urban Scale Surface Reconstruction

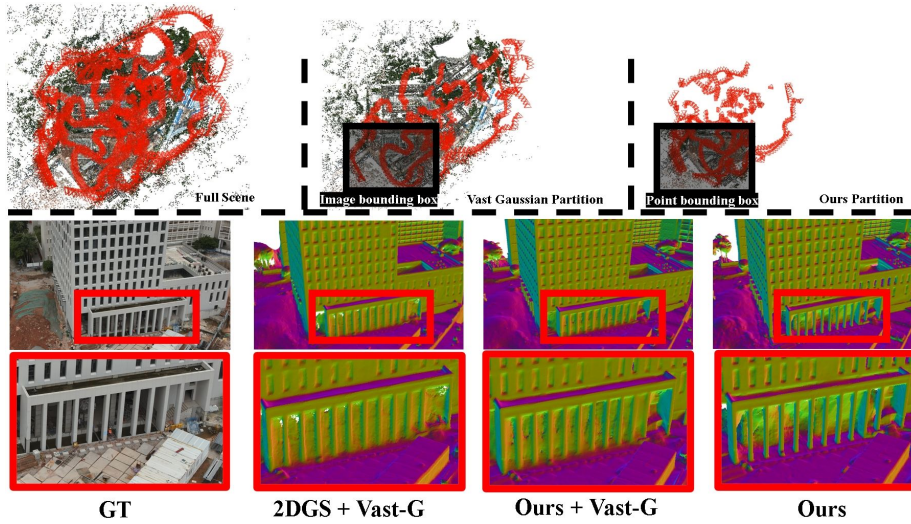


Figure 15: Qualitative comparison of partition strategies on a close-range dataset. The *black* bounding box is the same partition area. The image partition boundary for VastGaussian and the point cloud partition boundary for ULSR-GS are set to the same size according to the black boundary. Below are the meshes after clipping to the box size.

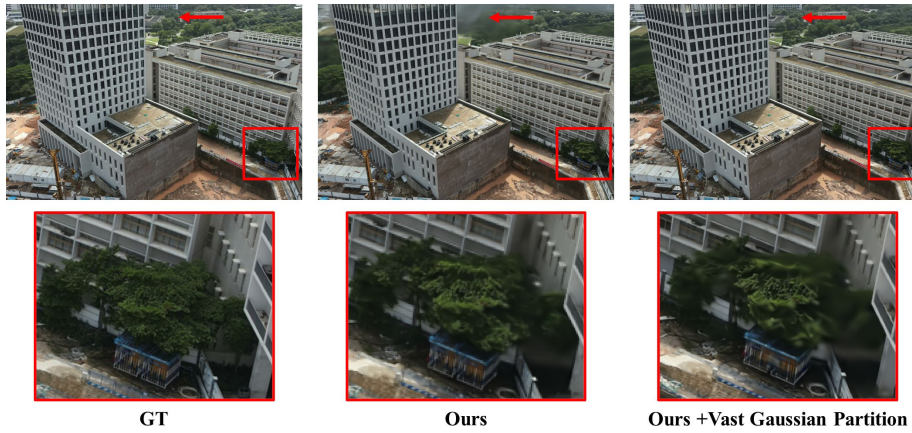


Figure 16: Qualitative comparison of partition strategies. In close-range photography tasks, a large number of background areas will appear. Our partitioning method emphasizes high-quality rendering of the reconstructed subject and ignores the division of background areas.

6. Discussion

6.1. Real World Application: Integration with USV Bathymetry model

We now discuss the ability of integrating the bathymetry digital elevation model (BDEM) obtained from single-beam echo sounder (SBES) with the oblique photogrammetric models produced by ULSR-GS to generate a real urban surface model. As shown in Figure 17 (a), the experimental site for this study is located at Moon Bay (Scene 2), situated along the southern shore of Dushu Lake in Suzhou, China. Moon Bay is a scenic and ecologically rich area, but it is also surrounded by a dense cluster of urban buildings, which presents significant challenges for UAV-based photogrammetric reconstruction and the subsequent data fusion with USV-derived bathymetric models.

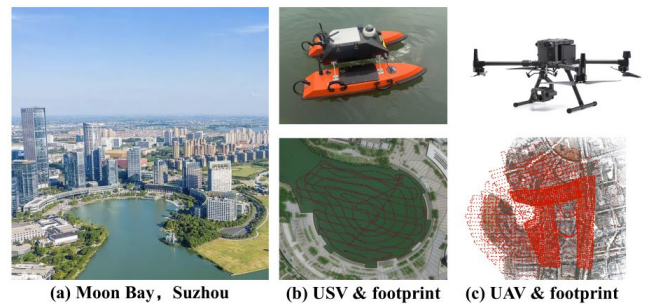


Figure 17: Experimental Location. (a) Bird-eye-view of the experimental location Moon Bay, Dushu Lake, Suzhou. (b) USV and its SBES bathymetry footprints. (c) UAV and its oblique photogrammetry footprints.

As shown in Figure 17 (b), the USV followed predefined paths across the water body, recording depth measurements at each point along its trajectory. The WGS-84 world coordinates were recorded with each measurement, providing a geospatial reference for each bathymetry point. Simultaneously, a UAV was deployed to capture oblique imagery of the surrounding landscape. Each image was georeferenced using the UAV’s embedded GPS, recording the WGS-84 world coordinates at the time of capture. The initial data consists of bathymetry measurements at specific points. The bathymetric data collected by the USV is first processed using Geographic Information System (GIS) software, where the raw measurements are converted into a DEM through Kriging interpolation. The high-resolution DEM is converted into a 3D mesh using standard Triangulated Irregular Network (TIN) algorithms. As shown in Figure 18, the ULSR-GS-generated mesh and the UAV-derived mesh are then aligned and merged. The alignment process ensures that both meshes are represented in the same global coordinate system (WGS-84 Mercator projection), allowing for seamless integration.

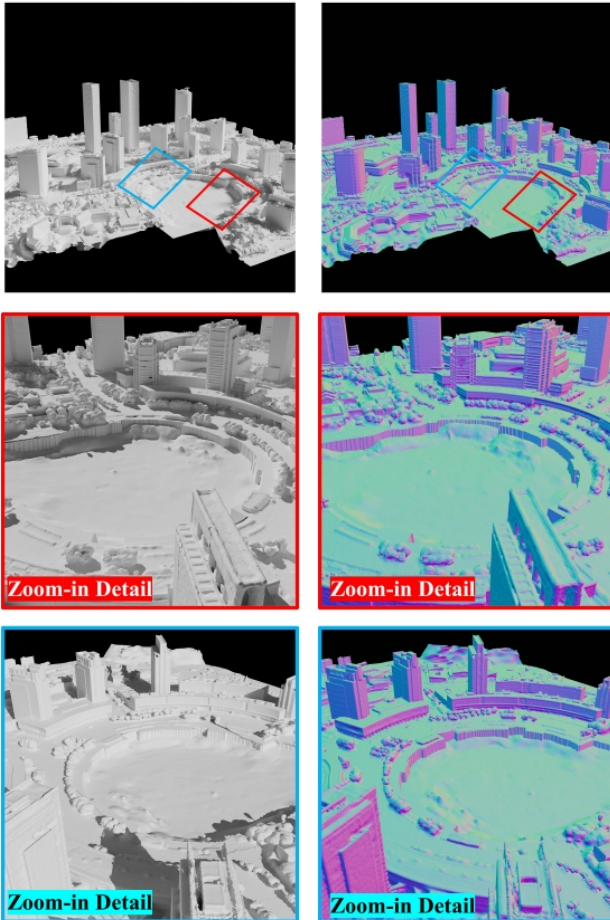


Figure 18: Zoomed-in detail of the fusion USV and UAV models. Left: Mesh; Right Normal.

6.2. Strength and Limitations

Our proposed ULSR-GS framework demonstrates notable advantages and specific application scenarios that

clearly distinguish it from existing single-GPU [15, 16, 66, 68, 5], multi-GPU [34, 30], and MVS-based [44] methods. Compared to single-GPU Gaussian Splatting (GS) approaches, ULSR-GS exhibits exceptional scalability and efficiency, making it particularly suitable for large-scale urban reconstruction tasks. The inherent memory constraints of single-GPU methods severely limit their capacity for handling extensive datasets; our multi-GPU strategy circumvents this limitation by employing an optimized point-to-photo partitioning technique driven by SfM. Consequently, ULSR-GS effectively reconstructs detailed urban scenes at scales previously unattainable with single-GPU methods [15, 16, 66, 68, 5].

Furthermore, compared with other multi-GPU GS approaches [34, 30] that typically rely on image-centric partitioning, ULSR-GS provides greater adaptability and accuracy, especially beneficial in complex scenarios such as close-range and oblique photogrammetry. Our innovative per-point partitioning ensures that each sub-region is reconstructed using its most relevant image set, thus addressing critical issues of uneven coverage and irregular camera paths encountered by traditional methods. These improvements are validated by quantitative metrics and qualitative evaluations across diverse urban scenes.

Moreover, relative to MVS-based methods [44], ULSR-GS is particularly effective in reconstructing thin and complex architectural structures, which often present significant challenges for correspondence-based MVS techniques due to matching ambiguities or limited local texture.

Despite these strengths, ULSR-GS also exhibits several limitations: (1) As shown in Figure 10, the framework is less effective in vegetation-rich environments, where dense correspondence-based MVS techniques better capture the intricate and semi-transparent structures inherent in foliage. (2) The generated meshes tend to be overly smooth, potentially lacking essential high-frequency geometric details needed for accurately representing intricate textures and detailed surfaces. (3) The current GS-based training and rendering resolution limit (approximately 1.6K) is insufficient for applications demanding high-detail fidelity, such as high-resolution (2cm per pixel) oblique photogrammetry. (4) Additionally, the existing depth-projection-based densification strategy primarily enhances regions already adequately reconstructed, inadequately addressing areas that are initially sparse or poorly captured.

7. Conclusion

We present ULSR-GS, a framework dedicated to high-fidelity surface extraction in ultra-large-scale scene. Specifically, our partitioning approach combines with a multi-view selection strategy. Additionally, ULSR-GS employs a multi-view geometric consistency densification to enhance surface details. Experimental results demonstrate that ULSR-GS outperforms other SOTA GS-based works on large-scale benchmark datasets. Our approach addresses key limitations

of image-based partitioning methods [29, 33, 20] by ensuring finer granularity in mesh boundaries and prioritizing the reconstruction of key scene regions. This strategy enables us to extract meshes individually rather than merge sub-regions and extract the full scene. Unlike existing MVS-based approaches, our method enables the simultaneous generation of a high-quality radiance field for rendering and a detailed mesh representation for reconstruction, all within a single training pipeline. Also, comparison with traditional MVS-based methods demonstrates ULSR-GS drastically reduces processing time while maintaining fine structural details. These advantages make ULSR-GS a promising choice for oblique photogrammetry, offering an efficient and scalable solution for real-world applications.

For future work, we identify three key directions to enhance our framework. First, improving depth computation will be crucial for refining surface extraction and reducing artifacts in complex environments. Second, developing highly efficient 4K-resolution rendering and surface extraction will address the current limitations of GS-based methods in photogrammetric applications. Finally, aerial and terrestrial photogrammetry are combined to complete the detailed reconstruction of the building facade structure while solving the surface reconstruction of the translucent glass building.

8. Acknowledgements

This work was supported by the Suzhou Municipal Key Laboratory for Intelligent Virtual Engineering (SZS2022004), the XJTLU AI University Research Centre, the Jiangsu Province Engineering Research Centre of Data Science and Cognitive Computation at XJTLU, and the SIP AI Innovation Platform (YZCXPT2022103).

References

- [1] Barron, J.T., Mildenhall, B., Tancik, M., Hedman, P., Martin-Brualla, R., Srinivasan, P.P., 2021. Mip-nerf: A multiscale representation for anti-aliasing neural radiance fields, in: Proceedings of the IEEE/CVF international conference on computer vision, pp. 5855–5864.
- [2] Barron, J.T., Mildenhall, B., Verbin, D., Srinivasan, P.P., Hedman, P., 2022. Mip-nerf 360: Unbounded anti-aliased neural radiance fields, in: Proceedings of the IEEE/CVF conference on computer vision and pattern recognition, pp. 5470–5479.
- [3] Bleyer, M., Rhemann, C., Rother, C., 2011. Patchmatch stereo-stereo matching with slanted support windows., in: Bmvc, pp. 1–11.
- [4] Cao, J., Wang, H., Chemerys, P., Shakhrai, V., Hu, J., Fu, Y., Makovichuk, D., Tulyakov, S., Ren, J., 2022. Real-time neural light field on mobile devices. arXiv preprint arXiv:2212.08057 .
- [5] Chen, D., Li, H., Ye, W., Wang, Y., Xie, W., Zhai, S., Wang, N., Liu, H., Bao, H., Zhang, G., 2024a. Pgsr: Planar-based gaussian splatting for efficient and high-fidelity surface reconstruction .
- [6] Chen, J., Ye, W., Wang, Y., Chen, D., Huang, D., Ouyang, W., Zhang, G., Qiao, Y., He, T., 2024b. Gigags: Scaling up planar-based 3d gaussians for large scene surface reconstruction. URL: <https://arxiv.org/abs/2409.06685>, arXiv:2409.06685.
- [7] Chen, M., Zhang, J., Xu, X., Liu, L., Cai, Y., Feng, J., Yan, S., 2022. Geometry-guided progressive nerf for generalizable and efficient neural human rendering, in: ECCV.
- [8] Chen, R., Han, S., Xu, J., Su, H., 2019. Point-based multi-view stereo network, in: Proceedings of the IEEE/CVF international conference on computer vision, pp. 1538–1547.
- [9] Chen, Y., Lee, G.H., 2024. Dogaussian: Distributed-oriented gaussian splatting for large-scale 3d reconstruction via gaussian consensus. URL: <https://arxiv.org/abs/2405.13943>, arXiv:2405.13943.
- [10] Chen, Y., Xu, H., Zheng, C., Zhuang, B., Pollefeys, M., Geiger, A., Cham, T.J., Cai, J., 2024c. Mvsplat: Efficient 3d gaussian splatting from sparse multi-view images. arXiv preprint arXiv:2403.14627 .
- [11] Cheng, K., Long, X., Yang, K., Yao, Y., Yin, W., Ma, Y., Wang, W., Chen, X., 2024. Gaussianpro: 3d gaussian splatting with progressive propagation, in: Forty-first International Conference on Machine Learning.
- [12] Çöltekin, A., Lochhead, I., Madden, M., Christophe, S., Devaux, A., Pettit, C., Lock, O., Shukla, S., Herman, L., Stachoň, Z., et al., 2020. Extended reality in spatial sciences: A review of research challenges and future directions. ISPRS International Journal of Geo-Information 9, 439.
- [13] Fan, L., Yang, Y., Li, M., Li, H., Zhang, Z., 2024. Trim 3d gaussian splatting for accurate geometry representation. arXiv preprint arXiv:2406.07499 .
- [14] Gao, J., Liu, J., Ji, S., 2023. A general deep learning based framework for 3d reconstruction from multi-view stereo satellite images. ISPRS Journal of Photogrammetry and Remote Sensing 195, 446–461. URL: <https://www.sciencedirect.com/science/article/pii/S0924271622003276>, doi:<https://doi.org/10.1016/j.isprs.2022.12.012>.
- [15] Guédon, A., Lepetit, V., 2023. Sugar: Surface-aligned gaussian splatting for efficient 3d mesh reconstruction and high-quality mesh rendering. arXiv preprint arXiv:2311.12775 .
- [16] Huang, B., Yu, Z., Chen, A., Geiger, A., Gao, S., 2024. 2d gaussian splatting for geometrically accurate radiance fields, in: SIGGRAPH 2024 Conference Papers, Association for Computing Machinery. doi:10.1145/3641519.3657428.
- [17] Kazhdan, M., Bolitho, M., Hoppe, H., 2006. Poisson surface reconstruction, in: Proceedings of the fourth Eurographics symposium on Geometry processing.
- [18] Kazhdan, M., Hoppe, H., 2013. Screened poisson surface reconstruction. ACM Transactions on Graphics (ToG) 32, 1–13.
- [19] Kerbl, B., Kopanas, G., Leimkühler, T., Drettakis, G., 2023. 3d gaussian splatting for real-time radiance field rendering. ACM Transactions on Graphics 42. URL: <https://repo-sam.inria.fr/fungraph/3d-gaussian-splatting/>.
- [20] Kerbl, B., Meuleman, A., Kopanas, G., Wimmer, M., Lanvin, A., Drettakis, G., 2024. A hierarchical 3d gaussian representation for real-time rendering of very large datasets. ACM Transactions on Graphics 43. URL: <https://repo-sam.inria.fr/fungraph/hierarchical-3d-gaussians/>.
- [21] Knapitsch, A., Park, J., Zhou, Q.Y., Koltun, V., 2017. Tanks and temples: Benchmarking large-scale scene reconstruction. ACM Transactions on Graphics (ToG) 36, 1–13.
- [22] Lang, I., Manor, A., Avidan, S., 2020. SampleNet: Differentiable Point Cloud Sampling, in: Proceedings of the IEEE/CVF Conference on Computer Vision and Pattern Recognition (CVPR), pp. 7578–7588.
- [23] Lee, D.T., Schachter, B.J., 1980. Two algorithms for constructing a delaunay triangulation. International Journal of Computer & Information Sciences 9, 219–242.
- [24] Li, S., Xiao, X., Guo, B., Zhang, L., 2020. A novel openmvs-based texture reconstruction method based on the fully automatic plane segmentation for 3d mesh models. Remote Sensing 12, 3908.
- [25] Li, Y., Jiang, L., Xu, L., Xiangli, Y., Wang, Z., Lin, D., Dai, B., 2023a. Matrixcity: A large-scale city dataset for city-scale neural rendering and beyond. arXiv e-prints , arXiv:2308.
- [26] Li, Z., Müller, T., Evans, A., Taylor, R.H., Unberath, M., Liu, M.Y., Lin, C.H., 2023b. Neuralangelo: High-fidelity neural surface reconstruction, in: Proceedings of the IEEE/CVF Conference on Computer Vision and Pattern Recognition, pp. 8456–8465.

- [27] Li, Z., Yao, S., Chu, Y., Garcia-Fernandez, A.F., Yue, Y., Lim, E.G., Zhu, X., 2024. Mvg-splatting: Multi-view guided gaussian splatting with adaptive quantile-based geometric consistency densification. URL: <https://arxiv.org/abs/2407.11840>, arXiv:2407.11840.
- [28] Liao, Y., Zhang, X., Huang, N., Fu, C., Huang, Z., Cao, Q., Xu, Z., Xiong, X., Cai, S., 2024. High completeness multi-view stereo for dense reconstruction of large-scale urban scenes. *ISPRS Journal of Photogrammetry and Remote Sensing* 209, 173–196. URL: <https://www.sciencedirect.com/science/article/pii/S0924271624000273>, doi:<https://doi.org/10.1016/j.isprsjprs.2024.01.018>.
- [29] Lin, J., Li, Z., Tang, X., Liu, J., Liu, S., Liu, J., Lu, Y., Wu, X., Xu, S., Yan, Y., Yang, W., 2024a. Vastgaussian: Vast 3d gaussians for large scene reconstruction, in: *Proceedings of the IEEE/CVF Conference on Computer Vision and Pattern Recognition (CVPR)*, pp. 5166–5175.
- [30] Lin, J., Li, Z., Tang, X., Liu, J., Liu, S., Liu, J., Lu, Y., Wu, X., Xu, S., Yan, Y., Yang, W., 2024b. Vastgaussian: Vast 3d gaussians for large scene reconstruction, in: *CVPR*.
- [31] Liu, J., Gao, J., Ji, S., Zeng, C., Zhang, S., Gong, J., 2023. Deep learning based multi-view stereo matching and 3d scene reconstruction from oblique aerial images. *ISPRS Journal of Photogrammetry and Remote Sensing* 204, 42–60. URL: <https://www.sciencedirect.com/science/article/pii/S0924271623002289>, doi:<https://doi.org/10.1016/j.isprsjprs.2023.08.015>.
- [32] Liu, J., Han, S., Li, J., 2024a. Mesh refinement method for multi-view stereo with unary operations. *ISPRS Journal of Photogrammetry and Remote Sensing* 218, 361–375. URL: <https://www.sciencedirect.com/science/article/pii/S0924271624004003>, doi:<https://doi.org/10.1016/j.isprsjprs.2024.10.023>.
- [33] Liu, Y., Guan, H., Luo, C., Fan, L., Wang, N., Peng, J., Zhang, Z., 2024b. Citygaussian: Real-time high-quality large-scale scene rendering with gaussians. arXiv preprint arXiv:2404.01133.
- [34] Liu, Y., Luo, C., Mao, Z., Peng, J., Zhang, Z., 2025. Citygaussianv2: Efficient and geometrically accurate reconstruction for large-scale scenes, in: *ICLR*.
- [35] Liu, Y., Xue, F., Huang, H., 2021. Urbanscene3d: A large scale urban scene dataset and simulator arXiv:2107.04286.
- [36] Lorensen, W.E., Cline, H.E., 1998. Marching cubes: A high resolution 3d surface construction algorithm, in: *Seminal graphics: pioneering efforts that shaped the field*, pp. 347–353.
- [37] Lu, T., Yu, M., Xu, L., Xiangli, Y., Wang, L., Lin, D., Dai, B., 2024. Scaffold-gs: Structured 3d gaussians for view-adaptive rendering, in: *Proceedings of the IEEE/CVF Conference on Computer Vision and Pattern Recognition*, pp. 20654–20664.
- [38] Mi, Z., Xu, D., 2023. Switch-nerf: Learning scene decomposition with mixture of experts for large-scale neural radiance fields, in: *International Conference on Learning Representations (ICLR)*. URL: <https://openreview.net/forum?id=PQ2zoIZqvm>.
- [39] Mildenhall, B., Srinivasan, P.P., Tancik, M., Barron, J.T., Ramamoorthi, R., Ng, R., 2021. Nerf: Representing scenes as neural radiance fields for view synthesis. *Communications of the ACM* 65, 99–106.
- [40] Oechsle, M., Peng, S., Geiger, A., 2021. Unisurf: Unifying neural implicit surfaces and radiance fields for multi-view reconstruction arXiv:2104.10078.
- [41] Palma, G., Boubekeur, T., Ganovelli, F., Cignoni, P., 2018. Scalable non-rigid registration for multi-view stereo data. *ISPRS Journal of Photogrammetry and Remote Sensing* 142, 328–341. URL: <https://www.sciencedirect.com/science/article/pii/S0924271618301746>, doi:<https://doi.org/10.1016/j.isprsjprs.2018.06.012>.
- [42] Pan, X., Lin, Q., Ye, S., Li, L., Guo, L., Harmon, B., 2024. Deep learning based approaches from semantic point clouds to semantic bim models for heritage digital twin. *Heritage Science* 12, 65.
- [43] Rusinkiewicz, S., Levoy, M., 2001. Efficient variants of the icp algorithm, in: *Proceedings Third International Conference on 3-D Digital Imaging and Modeling*, pp. 145–152. doi:10.1109/IM.2001.924423.
- [44] Schönberger, J.L., Zheng, E., Pollefeys, M., Frahm, J.M., 2016. Pixel-wise view selection for unstructured multi-view stereo, in: *European Conference on Computer Vision (ECCV)*.
- [45] Su, W., Tao, W., 2023. Efficient edge-preserving multi-view stereo network for depth estimation, in: *Proceedings of the AAAI Conference on Artificial Intelligence*, pp. 2348–2356.
- [46] Tancik, M., Casser, V., Yan, X., Pradhan, S., Mildenhall, B., Srinivasan, P., Barron, J.T., Kretzschmar, H., 2022. Block-NeRF: Scalable large scene neural view synthesis. arXiv.
- [47] Turki, H., Ramanan, D., Satyanarayanan, M., 2022. Mega-nerf: Scalable construction of large-scale nerfs for virtual fly-throughs, in: *Proceedings of the IEEE/CVF Conference on Computer Vision and Pattern Recognition*, pp. 12922–12931.
- [48] Turkulainen, M., Ren, X., Melekhov, I., Seiskari, O., Rahtu, E., Kannala, J., 2024. Dn-splatter: Depth and normal priors for gaussian splatting and meshing. arXiv:2403.17822.
- [49] Wang, P., Liu, L., Liu, Y., Theobalt, C., Komura, T., Wang, W., 2021. Neus: Learning neural implicit surfaces by volume rendering for multi-view reconstruction. *NeurIPS*.
- [50] Werner, D., Al-Hamadi, A., Werner, P., 2014. Truncated signed distance function: experiments on voxel size, in: *Image Analysis and Recognition: 11th International Conference, ICIAR 2014, Vilamoura, Portugal, October 22–24, 2014, Proceedings, Part II 11*, Springer. pp. 357–364.
- [51] Wu, C., Yu, X., Ma, C., Zhong, R., Zhou, X., 2024a. Integrating geospatial data and street-view imagery to reconstruct large-scale 3d urban building models. *Transactions in GIS* 28, 1326–1352.
- [52] Wu, J., Li, R., Xu, H., Zhao, W., Zhu, Y., Sun, J., Zhang, Y., 2024b. Gomvs: Geometrically consistent cost aggregation for multi-view stereo, in: *Proceedings of the IEEE/CVF Conference on Computer Vision and Pattern Recognition*, pp. 20207–20216.
- [53] Xiangli, Y., Xu, L., Pan, X., Zhao, N., Rao, A., Theobalt, C., Dai, B., Lin, D., 2022. Bungeenerf: Progressive neural radiance field for extreme multi-scale scene rendering, in: *European conference on computer vision*, Springer. pp. 106–122.
- [54] Xiong, B., Zheng, N., Liu, J., Li, Z., 2024. Gauu-scene v2: Assessing the reliability of image-based metrics with expansive lidar image dataset using 3dgs and nerf. arXiv:2404.04880.
- [55] Xu, L., Xiangli, Y., Peng, S., Pan, X., Zhao, N., Theobalt, C., Dai, B., Lin, D., 2023. Grid-guided neural radiance fields for large urban scenes. arXiv:2303.14001.
- [56] Xu, Q., Kong, W., Tao, W., Pollefeys, M., 2022a. Multi-scale geometric consistency guided and planar prior assisted multi-view stereo. *IEEE Transactions on Pattern Analysis and Machine Intelligence* 45, 4945–4963.
- [57] Xu, Q., Tao, W., 2020. Planar prior assisted patchmatch multi-view stereo, in: *Proceedings of the AAAI Conference on Artificial Intelligence*, pp. 12516–12523.
- [58] Xu, Q., Xu, Z., Philip, J., Bi, S., Shu, Z., Sunkavalli, K., Neumann, U., 2022b. Point-nerf: Point-based neural radiance fields, in: *Proceedings of the IEEE/CVF conference on computer vision and pattern recognition*, pp. 5438–5448.
- [59] Yang, B., Chen, C., 2015. Automatic registration of uav-borne sequent images and lidar data. *ISPRS Journal of Photogrammetry and Remote Sensing* 101, 262–274. URL: <https://www.sciencedirect.com/science/article/pii/S0924271615000180>, doi:<https://doi.org/10.1016/j.isprsjprs.2014.12.025>.
- [60] Yang, S., Cai, G., Du, J., Chen, P., Su, J., Wu, Y., Wang, Z., Li, J., 2022. Connectivity-aware graph: A planar topology for 3d building surface reconstruction. *ISPRS Journal of Photogrammetry and Remote Sensing* 191, 302–314. URL: <https://www.sciencedirect.com/science/article/pii/S0924271622002027>, doi:<https://doi.org/10.1016/j.isprsjprs.2022.07.024>.
- [61] Yao, Y., Luo, Z., Li, S., Fang, T., Quan, L., 2018. Mvsnets: Depth inference for unstructured multi-view stereo, in: *Proceedings of the European conference on computer vision (ECCV)*, pp. 767–783.
- [62] Yariv, L., Gu, J., Kasten, Y., Lipman, Y., 2021. Volume rendering of neural implicit surfaces. *NeurIPS*.
- [63] Yariv, L., Hedman, P., Reiser, C., Verbin, D., Srinivasan, P.P., Szeliski, R., Barron, J.T., Mildenhall, B., 2023. Bakedsd: Meshing neural sdf

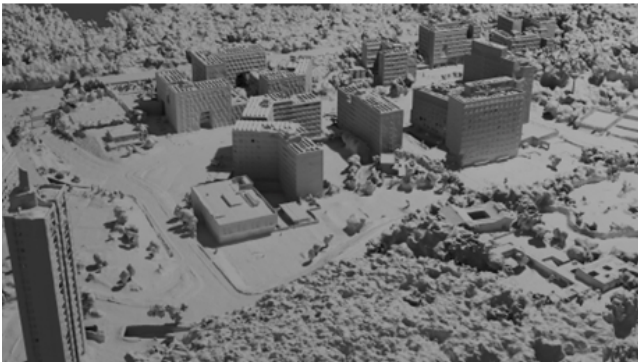
- for real-time view synthesis, in: ACM SIGGRAPH 2023 Conference Proceedings, pp. 1–9.
- [64] Yu, Z., Chen, A., Huang, B., Sattler, T., Geiger, A., 2024a. Mip-splatting: Alias-free 3d gaussian splatting, in: Proceedings of the IEEE/CVF Conference on Computer Vision and Pattern Recognition, pp. 19447–19456.
- [65] Yu, Z., Gao, S., 2020. Fast-mvsnet: Sparse-to-dense multi-view stereo with learned propagation and gauss-newton refinement, in: Proceedings of the IEEE/CVF conference on computer vision and pattern recognition, pp. 1949–1958.
- [66] Yu, Z., Sattler, T., Geiger, A., 2024b. Gaussian opacity fields: Efficient high-quality compact surface reconstruction in unbounded scenes. arXiv:2404.10772 .
- [67] Yu Chen, G.H.L., 2024. Dogaussian: Distributed-oriented gaussian splatting for large-scale 3d reconstruction via gaussian consensus, in: arXiv.
- [68] Zhang, B., Fang, C., Shrestha, R., Liang, Y., Long, X., Tan, P., 2024a. Rade-gs: Rasterizing depth in gaussian splatting. arXiv preprint arXiv:2406.01467 .
- [69] Zhang, K., Riegler, G., Snavely, N., Koltun, V., 2020. Nerf++: Analyzing and improving neural radiance fields. arXiv preprint arXiv:2010.07492 .
- [70] Zhang, S., Wei, Z., Xu, W., Zhang, L., Wang, Y., Zhang, J., Liu, J., 2024b. Edge aware depth inference for large-scale aerial building multi-view stereo. ISPRS Journal of Photogrammetry and Remote Sensing 207, 27–42. URL: <https://www.sciencedirect.com/science/article/pii/S0924271623003258>, doi:<https://doi.org/10.1016/j.isprsjprs.2023.11.020>.
- [71] Zhu, Z., Stamatopoulos, C., Fraser, C.S., 2015. Accurate and occlusion-robust multi-view stereo. ISPRS Journal of Photogrammetry and Remote Sensing 109, 47–61. URL: <https://www.sciencedirect.com/science/article/pii/S0924271615001999>, doi:<https://doi.org/10.1016/j.isprsjprs.2015.08.008>.



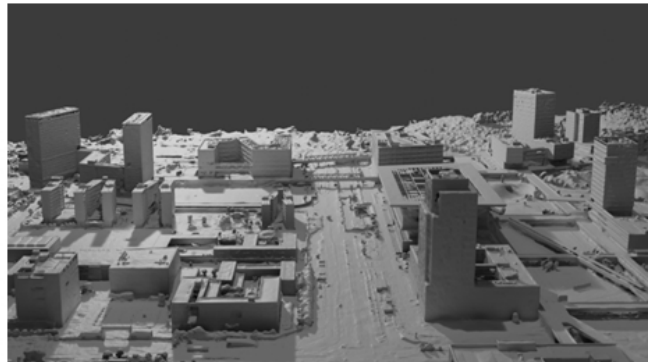
SMBU



LFLS



UPPER CAMPUS



SZTU



SciArt



Campus

Figure 19: Mesh Results on GauU-Scene [54] and UrbanScene 3D [35] Datasets.

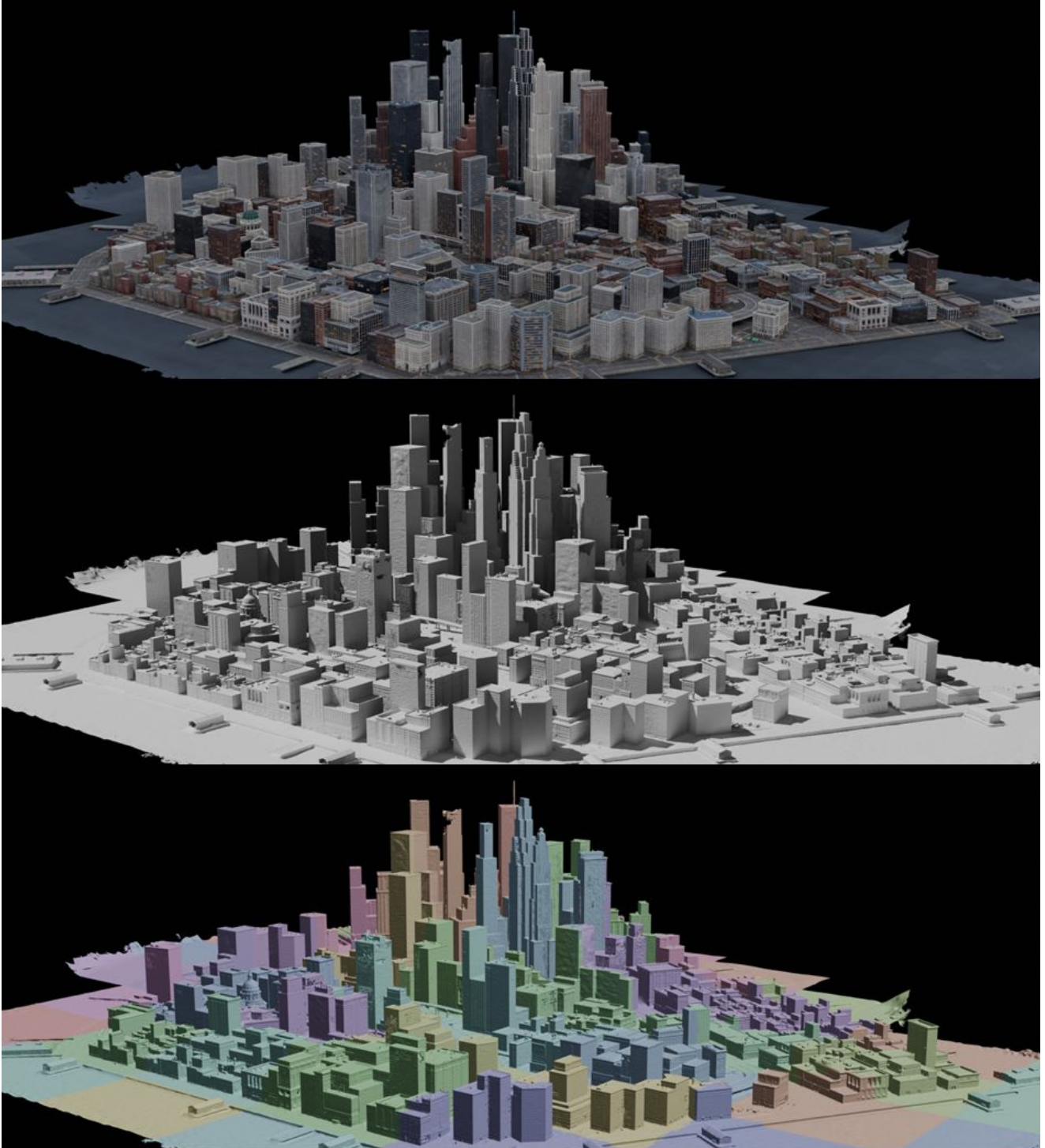


Figure 20: Mesh Results on MatrixCity [25] Dataset.



Figure 21: Mesh Results on Scene 1.

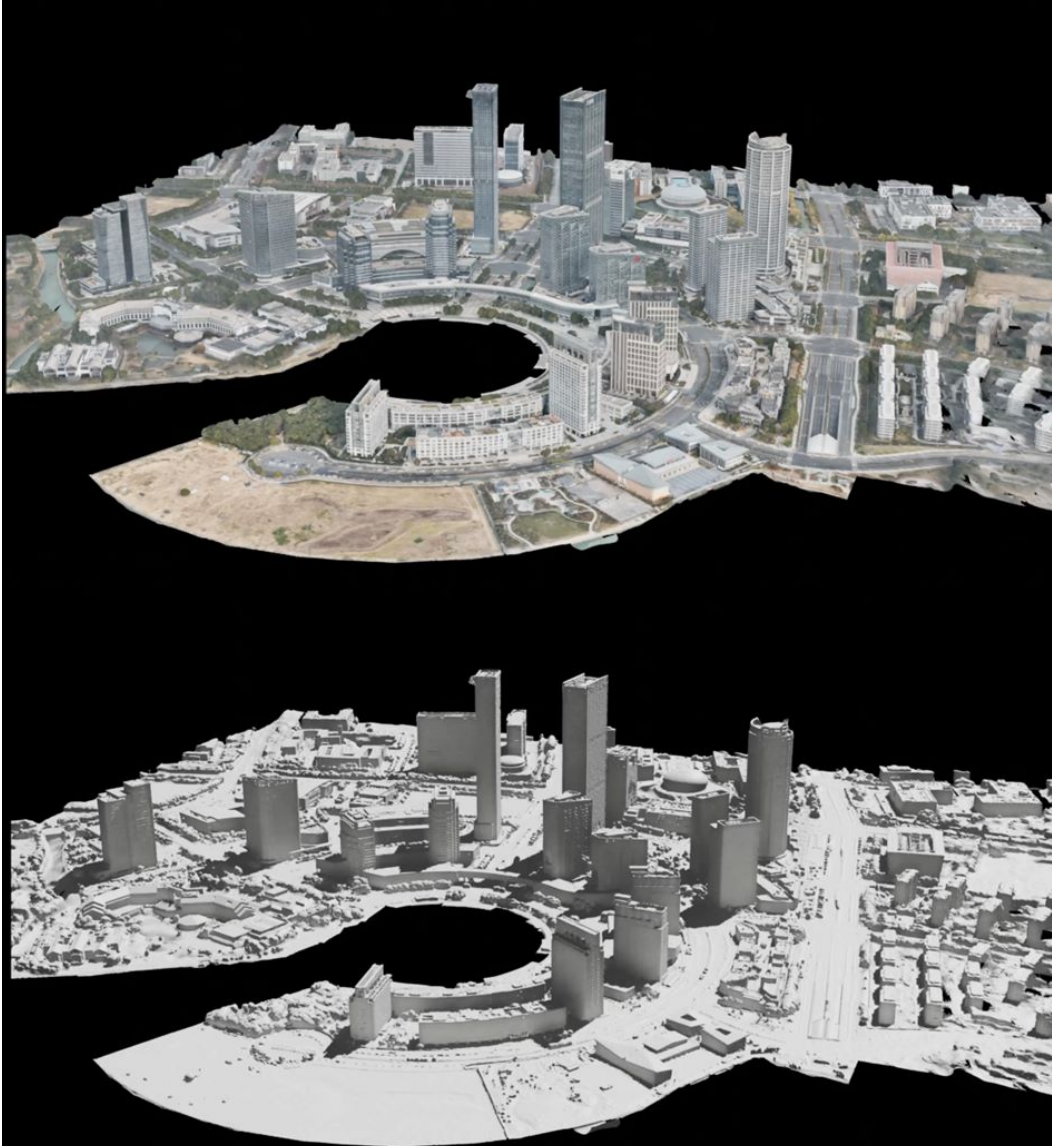


Figure 22: Mesh Results on Scene 2.